Effects of microstructure heterogeneity and defects on mechanical behavior of Zr modified AA7075 manufactured by laser powder bed fusion

Yongkang Luo[a1], Nicolas Nothomb[b1], Tianyan Yu[a], Lv Zhao[a,d,*], Julie Villanova[c], Zhenhuan Li[a,d], Aude Simar[b]

[a] *Department of Mechanics, School of Aerospace Engineering, Huazhong University of science and Technology, Wuhan, China*

[b] *Institute of Mechanics, Materials and Civil Engineering, UCLouvain, Louvain-la-Neuve, Belgium*

[c] *ESRF - The European Synchrotron, Grenoble 38043, France*

[d] *Hubei Key Laboratory of Engineering Structural Analysis and Safety Assessment, 1037 Luoyu Road, Wuhan, China*

Abstract

Laser powder bed fusion of AA7075 is an ideal candidate for aerospace structures due to high structure design flexibility of the process and excellent strength-to-weight ratio of AA7075. Various inoculants have been incorporated into AA7075 to control solidification behavior and suppress hot cracks in literature, leading to notable microstructure heterogeneity, distinct defect characteristics and large scattering of mechanical performance. However, the way these microstructures and defects affect mechanical behaviors remains unexplored. The present work is devoted to decipher the correlation between microstructure/defects and mechanical properties of Zr modified AA7075 under as-built and T6 states. Tensile tests under different loading directions were performed with macroscale and microscale digital image correlation,

[1] These authors contributed equally to the work; * Corresponding author: lvzhao@hust.edu.cn (L. Zhao).

showing anisotropy in ductility and inhomogeneous strain distribution across solidified melt pools. It is noteworthy that the T6 heat treatment significantly enhances the strength while maintaining the ductility of the as-built state. The ductility anisotropy is related to sharp lack-of-fusion defects, and the bypass of strength-ductility trade-off in the T6 state is induced by strain delocalization in coarse grain regions containing sharp defects and the suppression of dense submicron pores in fine grain zones.

Keywords

Laser powder bed fusion; AA7075, Microstructure, Defect, Mechanical properties

1. Introduction

Metal additive manufacturing (AM, also known as 3D printing) is a revolutionary route for producing advanced materials and structures [1], owing to its specific thermal history leading to unique microstructure features [2] and its abilities to shape complex geometries broadening the design boundaries [3]. AM components have notable application prospects in many fields such as aeronautic, aerospace, biomedical industries, and quite many applications have been reported in literature, heralding the bright future of this advanced manufacturing technology [4].

Among the AM metals, aluminum alloys (AA) are ideal candidates for the harsh demand of lightweight structures, owing to their excellent strength-to-weight ratio. The most widespread AM Al alloys are Al-Si alloys [5] and derived metal matrix composites [6] because of their good printability. To pursue higher strength, tremendous efforts have been devoted to print other high strength Al alloys, such as the heat-treatable AA 7xxx that exhibit notable strengthening mechanisms, with a yield strength generally above 500 MPa. However, processing of 7xxx alloys exhibiting sufficient quality for application was unachievable, regardless of processing parameters of fusion-based additive manufacturing [7-10]. The biggest challenge is the hot cracking associated with long columnar grains. Solid-based approaches prevent many of the problems induced by the solid-liquid-solid phase transformations [11], but they also have limitations and currently still lack a degree of maturity. The hot-cracking issue was solved by the strategy stemming from Martin et al. [12], where ZrH_2 was introduced to the AA 7075 powder to control the solidification behavior during the laser melting process. Consequently, sub-micron precipitates of nucleants (Al_3Zr) were formed, promoting columnar-to-equiaxed (CTE) grain growth transition, suppressing hot cracks and achieving near full-density AA 7xxx. This approach unchoked the pathway to developing high strength AM Al alloys.

Inspired by the approach proposed by Martin et al. [12], many different nanoparticles and additions as well as processing parameters were explored for better controlling the solidification behavior and improving the mechanical properties of AM AA7xxx. The underlying mechanism is that the precipitated Al_3X (X represents the added element) or the added particles have very low lattice mismatch with the α-Al so that they can act as heterogeneous nucleation sites, leading to fine Al grains and preventing crack formation [13]. Jiang et al. [13] obtained crack-free Al-Zn-Mg-Cu alloy by adding TiH_2 particles, and showed a fully fine equiaxed grain structure (average size of 1 μm) granted by the Al_3Ti particles. Zhu et al. [14] incorporated Sc and Zr into Al-Zn-Mg-Cu alloy and manufactured crack-free samples with primary $Al_3(Sc_x,Zr_{1-x})$ particles acting as inoculants for ultrafine grains (down to 350 nm). Xiao et al. [15] modified the Al-Zn-Mg-Cu alloy with Nb nanoparticles, and the primary Al_3Nb particles were found to be the heterogeneous nucleation sites promoting fine grains (average size of 1.9 μm). Shi et al. [16] manufactured Hf modified Al-Zn-Mg-Cu alloy, with primary Al_3Hf particles triggering the CTE transition. Li et al. [17] added TiB_2 reinforcements in the Al-Zn-Mg-Cu powder and successfully printed crack free samples presenting equiaxed fine grains (average size of 2 μm). The authors argued that the heterogeneous nucleation event of Al grains was triggered by the added TiB_2 reinforcements instead of in-situ formed Al_3Ti particles. Liu et al. [18] proposed a synergistic grain-refining strategy by incorporation of TiC and TiH_2 particles, promoting heterogeneous nucleation from in-situ $L1_2$-Al_3Ti particles and restriction to grain growth from TiC particles. This synergistic strategy suppressed the hot cracking and generated very fine grain structure (average grain area of 1.5 μm^2).

The microstructure of inoculant-containing AA7xxx depends on the thermal condition within the melt pool liquid, the incubation time of the Al_3X phase and the inoculant contents. There are two typical microstructures reported in literature, i.e. fully fine equiaxed grains and bimodal (multimodal) grain structure. The latter generally consisted of fine equiaxed grains at melt pool borders and coarse columnar grains in melt pool interiors, see the schematic drawing in Fig. 1. Note that the term “melt pool” refers to the microstructure obtained after solidification of the fluid material in this paper, unless otherwise specified. In theory, the formation of the grain structure is related to the competitive nucleation between primary Al_3X and α-Al [19, 20].

When the cooling rate (or the solid-liquid interface velocity) is low, which is the case at the melt pool borders, the incubation time of the Al_3X phase is satisfied, leading to inoculants that in turn refine the α-Al grains. In contrast, when the cooling rate is high, which is typically the case in the melt pool interiors, the nucleation condition of the Al_3X phase is not met, the α-Al will directly nucleate from the liquid, forming columnar grains and trapping the added X elements as solid solution. Bimodal grain structures were frequently obtained in X modified Al-Zn-Mg-Cu alloy due to the steep difference of cooling rate between the melt pool border and interior [14, 20]. Nevertheless, the volume fraction of fine equiaxed grains could be tuned with inoculant elements and their contents. Xiao et al. [15] pointed out that the incubation time of Al_3Nb is shorter than that of other Al_3X (X=Ti, Sc), so Al_3Nb is expected to more effectively refine the grain size within the melt pools. Martin et al. [21] and Shi et al. [16] showed that a fully equiaxed structure could be obtained when increasing the inoculant content in a laser powder bed fusion (LPBF) Al-Zn-Mg-Cu alloy. This could be related to the increased constitutional undercooling favoring heterogeneous nucleation of Al_3X phase.

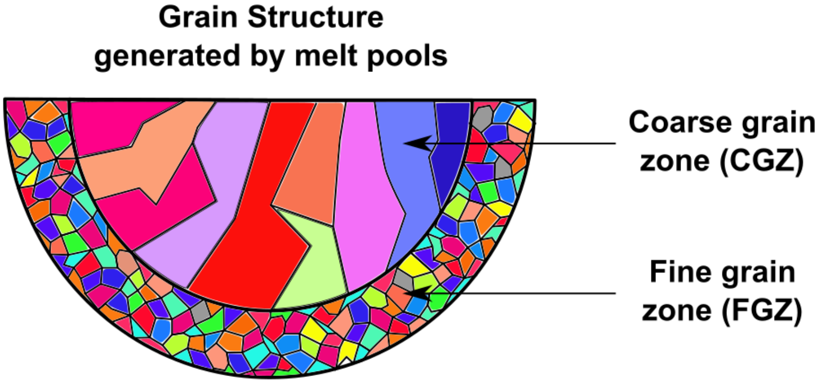

Fig. 1. Schematic of bimodal grain structure within solidified melt pool of Al3X-containing AA7xxx processed by laser powder bed fusion.

Table 1. Mechanical properties of X modified Al-Zn-Mg-Cu alloys

Inoculants	Yield strength (MPa)		Elongation to fracture		Reference
	As-built	T6 heat treatment	As-built	T6 heat treatment	
ZrH_2	-	325-373	-	3.8%-5.4%	[12]
TiH_2	292	496	4.8%	7.2%	[13]
Nb	332	412	17.1%	12.3%	[15]
Ti	190	420	7.9%	7.5%	[22]
Ta	≈250	-	5.1%	-	[23]
Er	≈200	-	15.9%	-	[24]
Si+Zr	397	-	6.5%	-	[25]
Sc+Zr	445	647	17.7%	11.6%	[14]
TiC+TiH_2	297	485	7.5%	10.0%	[18]
TiH_2+B	220	499	9.6%	12.8%	[26]
Metallic glass	488	-	9.0%	-	[27]
Wrought 7075	-	502	-	10.5%	[28]

As the chemical content (especially the added X elements) and process parameters differ from one study to another, the reported mechanical properties also present a notable scattering in terms of yield strength and ductility (or elongation to fracture), for both as-built state and after T6 heat treatment, see Table 1 (wrought AA7075-T6 also presented for comparison). In addition, most previous works focused on one loading direction in the tensile tests, whereas anisotropy was not assessed. Although strength was frequently assessed with theoretical strengthening models accounting for microstructure features, the coupling effects of microstructure and defects on damage and fracture were rarely addressed. From Table 1, it can be seen that the yield strength is mostly improved by T6 heat treatment, whereas the elongation to fracture either increases or decreases. Up to now, no works systematically assessed the structure/defect-mechanical property relationship and discussed the damage mechanism for as-built and heat treated states.

The present work is devoted to investigate the effects of microstructure heterogeneity and defects on the mechanical behavior of Zr modified AA7075 manufactured by laser powder bed fusion. Combining tensile tests and multi-scale digital image correlation analysis, both macroscopic mechanical properties and microscopic deformation and damage behaviors were assessed, based on which the ductility and its anisotropy were discussed and correlated to heterogeneous melt pool structure and lack-of-fusion defects. Moreover, the underlying mechanism for the bypass of the strength-ductility trade-off after T6 heat treatment is explained.

2. Materials and experiments

2.1 Material manufacturing

The pre-alloyed AA7075 powder was mechanically mixed with 2wt% ZrH_2 powder using a turbula mixer for six hours. The ZrH_2 powder serves to form Al_3Zr nucleants, allowing to prevent hot cracking. The powder feedstock is the same as in our related work [29]. The precise chemical composition was obtained by inductively coupled plasma optical emission spectroscopy (ICP-OES, Agilient Technologies 5100, USA), as presented in Table 2. The size distribution of the AA7075 powder is d_{10} = 21 μm, d_{50}= 38 μm and d_{90} = 63 μm, and it is d_{10} = 3 μm, d_{50} = 14 μm and d_{90}= 36 μm for the ZrH_2 powder. The Zr modified AA7075 (AA7075+1.8wt%Zr) samples were manufactured through LPBF by a ProX®DMP 200 system (3D Systems Inc., USA). Plates of 5×35×150 mm were printed on a non-heated squared Al5Mg (wt%Mg) build-plate of size 141 mm×141 mm (see Fig. 2c). The processing parameters were as follows: laser power = 164 W, layer thickness = 30 μm, hatch spacing = 50 μm, scanning speed = 400 mm/s and 90° scan rotation between layers. A pre-sintering scanning strategy was employed, i.e. each layer was scanned twice, the first scan used half the power (82 W) and the second the full power (164W), see the schematic drawing in Fig. 2a. The selection of the process parameters and pre-sintering strategy has been rationalized in our recent work [29]. After printing, the plates were removed from the build-plate using electrical discharge machining, and subjected to a T6 heat treatment, which involved a solid solution at 425 °C for 1h, followed by water quenching and an artificial aging at 120 °C for 24h. The selection of the LPBF process parameters and the T6 parameters was justified in our related works [29, 30]. The chemical composition of the printed sample was also measured and presented in Table 2. It can be seen that there are significant losses of Mg and Zn due to elements' preferential vaporization during the LPBF process.

Table 2. Chemical compositions (wt%) of the mixed powder and the printed sample.

	Al	Cr	Cu	Fe	Mg	Zn	Zr	Mg loss	Zn loss
Mixed powder	bal	0.21	1.53	0.08	2.38	5.30	1.87	-	-
LPBF sample	bal	0.22	1.55	0.10	1.68	3.16	1.77	29%	40%

2.2 Microstructure and defect characterizations

Scanning electron microscopy (SEM) was used to characterize the microstructure and defects of the LPBF AA7075-Zr samples in as-built and T6 states. Metallurgical polishing was performed to obtain appropriate surface quality. The sample preparation includes grinding with SiC papers, polishing with diamond suspension (15 μm and 3 μm) and oxide polishing suspension (OPS) for 2 h. The observations were conducted with JSM-IT500A equipment (Jeol, Japan). The backscatter electron diffraction mode was employed to obtain a better phase contrast. A large number of SEM images was acquired to statistically assess the defect size, orientation and distribution. ImageJ was used for image post-treatment. In addition, electron backscatter diffraction (EBSD) characterization of the as-built sample was performed to assess the grain size and orientation distribution. The EBSD was performed with an Oxford Symmetry detector (Oxford, UK), with a step size of 0.2 μm. The post-treatment of EBSD data was conducted with the AZtecCrytal software (version 2.1.2).

The addition of ZrH_2 might induce massive tiny pores in the built AA7075 due to decomposed hydrogen. To assess the evolution of such pores during the T6 heat treatment, X-ray nano-holo-tomography experiments (nano-CT) were performed on beamline ID16B at the ESRF synchrotron (Grenoble France) [31]. The nano-CT samples exhibited a cross section of 300 μm × 300 μm. The volumes with a field of view of 61 μm × 61 μm × 70 μm were acquired with a pixel size of 35nm in the middle of the samples. A full holo-tomographic scan consists of performing tomographic scans at four different propagation distances [32]. For each scan, a total of 3203 projections were taken on a PCO edge 4.2 camera over the 360° rotation for each scan with a beam energy of 29.6 keV, a wavelength of 0.042 nm and a counting time of 0.05 s per image. A dedicated furnace was implemented in the nano-CT setup, allowing to perform the heat treatment (425 °C for 1h) without moving the sample. Therefore, the same region of interest was scanned before and after the heat treatment. Exactly the same scanning parameters were used for the scans before and after the heat treatment. Subsequently, reconstruction of the volumes was performed using an ESRF in-house phase retrieval code using a delta/beta of 150 and PyHST2 software with filtered back-projection reconstruction [33]. Using Avizo software

(ThermoSientific, USA), the two scans (before and after the heat treatment (HT)) were aligned to be able to perform pore tracking. Based on the 3D data, the pore equivalent diameter was obtained following this formula: $d_{equi} = \sqrt[3]{3V/4\pi}$ (V represents the pore volume). The pores larger than 105 nm (i.e. 3 times the voxel size) were segmented from the nano-CT scans. Note that only the pores larger than 1 μm were tracked individually before and after the heat treatment since the smaller ones were too difficult to track and mostly healed during the HT. The same segmentation parameters were used for the AB and HT conditions.

2.3 Mechanical tests

Given the heterogeneous nature of the melt pool structure of LPBF AA7075-Zr, nanoindentation was first conducted with a Hysitron TI980 equipment (Bruker, Germany) to assess the local hardness and its correlation to grain structure. The indentation was performed under load control, the maximum force was 5 mN and the dwell time was 2 seconds. A matrix of 20×30 indents was obtained, with a spacing of 5 μm. Note that this spacing should be large enough to prevent neighboring indents to affect hardness values, as it is more than ten times the indentation depth (350-400 nm) [34]. The average nanohardness for different melt pool regions was then calculated, with the aid of EBSD.

To assess the strength and ductility of the LPBF AA7075-Zr samples, uniaxial tensile tests were performed along two loading directions, one parallel (namely horizontal (H)) and the other perpendicular (namely vertical (V)) to the building direction, respectively, see Fig. 2b and c. Two tensile samples (1.5 mm thick) were extracted from the mid-plane of the build, so one of the sample surfaces is 1 mm away from the build's external surface (Fig. 2c). Only small samples were used in the present work, as standard tensile samples in the vertical direction cannot be obtained with the printed plates due to their limited width (36 mm, see Fig. 2c). Note that the mechanical properties obtained with standard samples in the horizontal direction were reported in a related work [30]. The tensile tests were performed with a Deben tensile stage (MT2000, Deben, UK), using a loading speed of 0.05 mm/min. To measure the macroscale and microscale strain distributions by digital image correlation (DIC), two individual sets of speckle patterns (they do not overlap) were deposited on the sample surface, the first was achieved with matte paint (white paint for the background and black paint for the speckles) speckle pattern (macro-DIC) (see Fig. 2d), and the second with the nanoscale gold particles (HR-DIC, HR represents high resolution) (see Fig. 2e). The deposition of the gold particles was realized with an ion sputter equipment (ISC150, Supro Instruments, China) at a power of 6W and spraying time of 160s, inspired by the works of Hoefnagels et al. [35] and Vermeij and Hoefnagels [36]. Such deposition is performed at room temperature so that the microstructure of LPBF AA7075-Zr will not be affected. The average diameter of the gold particles is about 200 nm. These evenly distributed gold particles allow for quantitative assessment of strain field in different regions of melt pools.

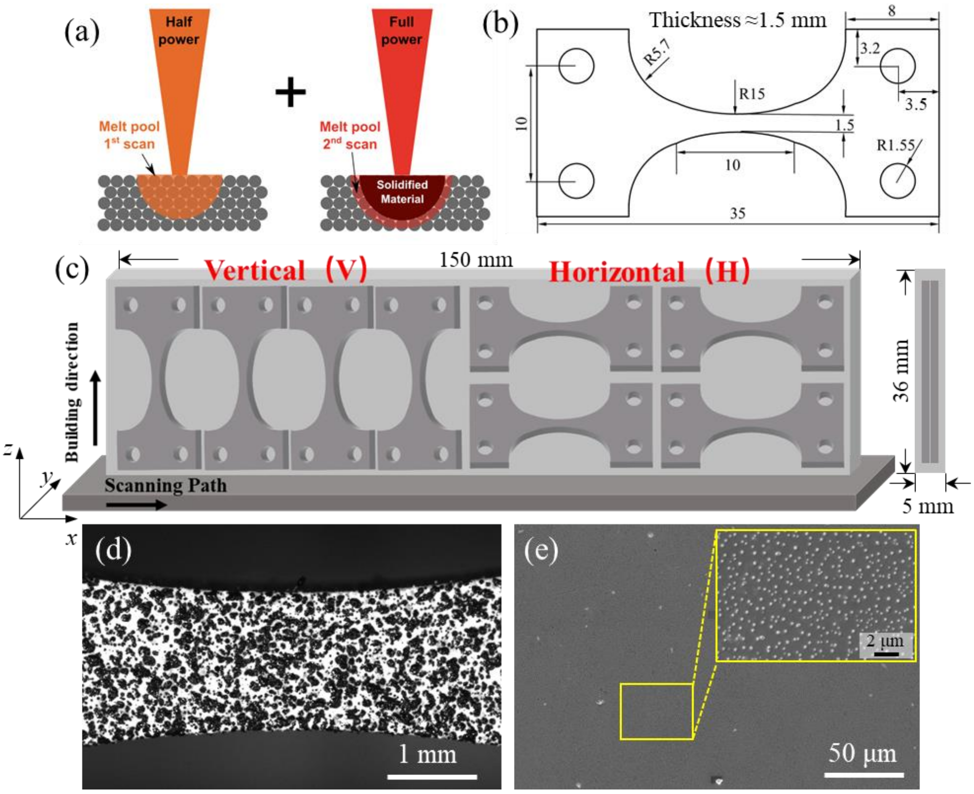

Fig. 2. Schematic of pre-sintering scanning strategy (a), tensile sample size (b), extraction of tensile samples from printed plate (c), speckle patterns for macroscale DIC (d) and microscale DIC (e) analyses. The 10 mm long region in (b) is the reduced section. All dimensions in (b) are in mm.

The speckle pattern deformation was tracked by an industrial camera (Baumer VCXG-25M) and an SEM (JSM-IT500A, Jeol, Japan) for the macroscale and microscale strain field measurements, respectively. At least three samples were tested for macro DIC until fracture. Moreover, interrupted tensile tests were carried out to assess damage behaviors close to final failure. For the in-situ SEM HR-DIC tests, a series of 5120×4096 pixel high-resolution (50 nm/pixel) SEM images was acquired at different deformation levels. It is noteworthy that two images were taken at each step to obtain a sufficiently large region of interest (roughly 250× 300 μm^2). All DIC analyses were performed with the open-source code Ncorr [37].

3. Results

3.1 Microstructure features

Representative microstructural features are shown in Fig. 3. Both the as-built (AB) and T6 samples (*xz*-plane, extracted approximately from the center of the build) present bimodal (sometimes called trimodal if medium grains are identified) grain structures, i.e. the melt pool interiors and borders are composed of large columnar and fine equiaxed grains, respectively, whose boundaries are indicated by the dashed lines in Fig. 3a and d. In the rest of the paper, these two regions are referred to as coarse grain zone (CGZ) and fine grain zone (FGZ). In the AB state (see Fig. 3b and c), the grains are all enclosed by a precipitate network rich in Zn, Mg and Cu, as shown in detail in our related work [30]. These precipitates are dissolved during the T6 heat treatment. The white precipitates (i.e. secondary particles) present in the CGZ after the HT (see Fig. 3e) have been identified in our related work [30] as a complex population of precipitates: Al_7Cu_2Fe intermetallics preferentially located at the grain boundaries, and both $Al_{18}Mg_3Cr_2$ dispersoids and Mg oxides inside the grains. The same precipitates can also be observed in the FGZ after the HT (see Fig. 3f). Additionally to the abovementioned phases, inside the FGZ for both conditions, $L1_2$-Al_3Zr particles can be observed (see the inset of Fig. 3c), they precipitate prior to α-Al at the melt pool borders and serve as heterogeneous nucleation sites of Al grains [12].

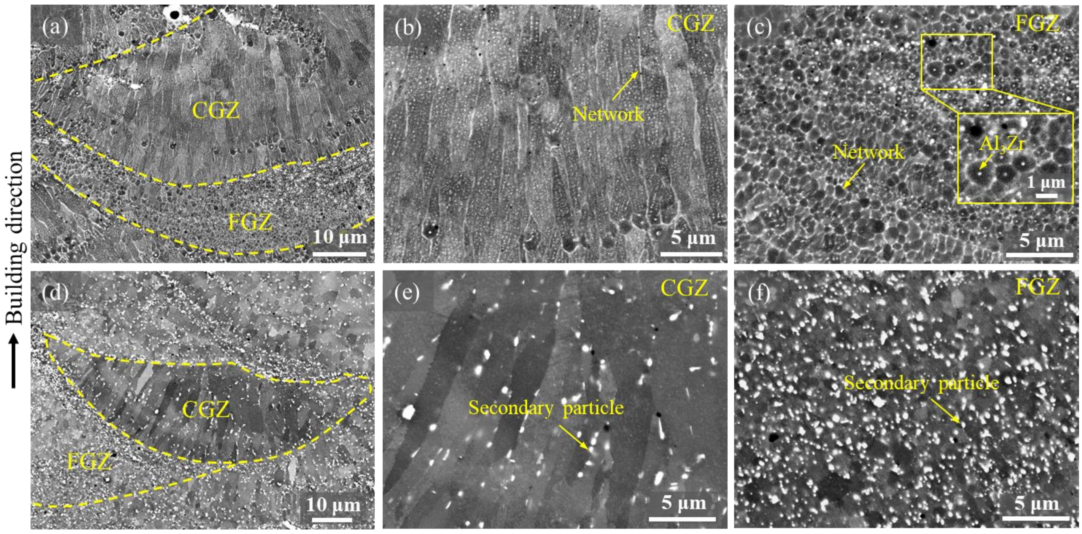

Fig. 3. Microstructural features (*xz*-plane) of the as-built sample (a-c) and the T6 sample (d-f). The dashed lines in (a) and (d) indicate the boundaries between the large columnar and fine equiaxed grain zones.

Besides the typical CGZ and FGZ microstructures, specific microstructure bands are observed throughout the as-built sample, as shown by Fig. 4a. Such band separates two CGZs, accompanied by an orientation change of the columnar grains as well as the grain boundary (GB) precipitate network. In this sense, these specific bands presumably belong to the border separating two melt pools given the abrupt change of thermal gradient. As such bands are not systematically present in all CGZs, they are probably generated by the pre-sintering step (half laser power). To verify this conjecture, one sample was finished (i.e. the last layer) intentionally with only the pre-sintering step. From Fig. 4c and d, it can be seen that the melt pool borders of the last layer resemble the specific bands shown in Fig. 4a. According to the statistics of the melt pool depth (Fig. S1 in the supplementary material), the average depth for the second full-power laser scan is 74 ± 24 µm. Nevertheless, the layer thickness generated by the first half-power laser scan can locally exceed 100 µm, indicating that the melt pool borders of the pre-sintering step may partially persist during the full-power laser scan. It is noteworthy that such specific bands disappear in the T6 sample due to microstructure homogenization, as can be seen in Fig. 4b where the dashed ellipse encircles a “boundary” separating two CGZs. This boundary should be a specific band originally present in the AB state.

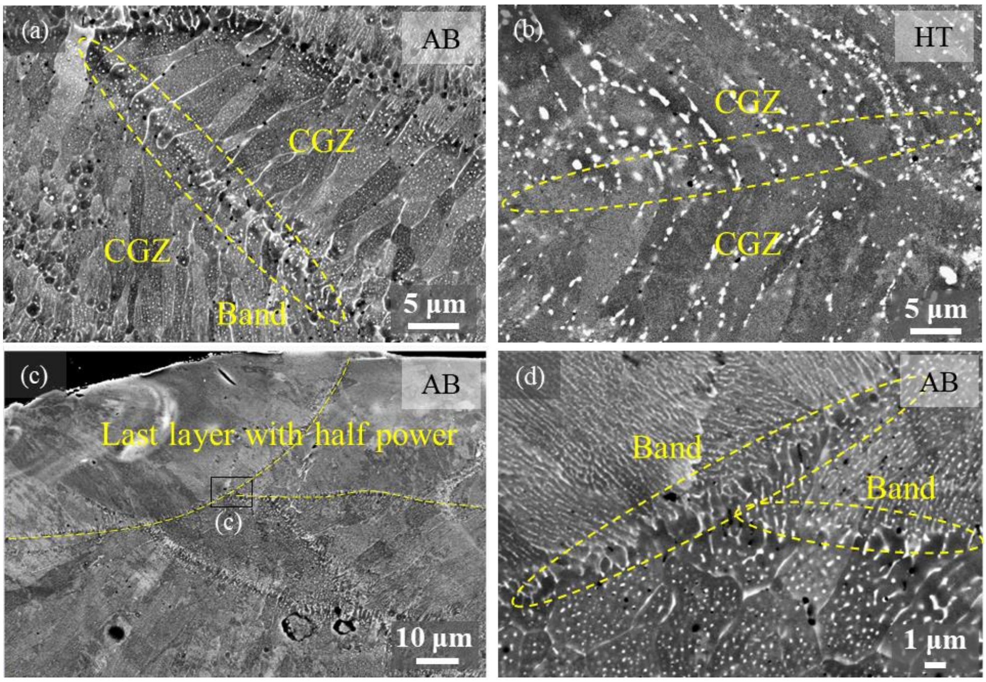

Fig. 4. Specific bands in the as-built sample (a), band disappearance in the heat treated sample (b), microstructure of the last layer scanned with only half laser power (c), bands at melt pool borders of the last layer (d). These microstructures correspond to the *xz*-plane. The dashed ellipses in (a) and (d) indicate the specific bands in the AB sample, and the dashed ellipse in (b) indicates the band dissolution in the HT sample. The dashed lines in (b) indicate the melt pool borders.

According to our previous work on the same material [30], the fine equiaxed grains incorporating Al_3Zr particles generally have an equivalent diameter smaller than 2 μm. Therefore, the grains characterized by EBSD are divided into two subgroups, one for large grains (≥2 μm) and the other for small grains (<2 μm), as shown in Fig. 5 (sample extracted from the center of the build). The two grain regions present a very close area fraction (both at

50%). It is noteworthy that the selected 2 μm is a more or less arbitrary value to define the upper limit of the grain size in the FGZ. Nevertheless, as shown in Fig. 5, it allows to clearly separate the melt pool borders from the melt pool interiors. The same or close (2 μm or 1.5 μm) size criterion for the definition of grain populations has been used in literature for LPBF high-strength Al alloys [14, 19, 38]. Besides the difference in size, it is found that some large columnar grains present preferential orientation along the building direction (BD), which is also reflected by the inverse pole figure for the z direction (see Fig. 5a). Nevertheless, such orientation relation is not a generality for all columnar grains. As for the fine grains, a quite random orientation distribution is revealed, as can be seen from the inverse pole figures in Fig. 5b. The preferential orientation of the long columnar grains can be related to the thermal gradient pointing toward the melt pool center. Such phenomenon is frequently reported for LPBF Al alloys [5].

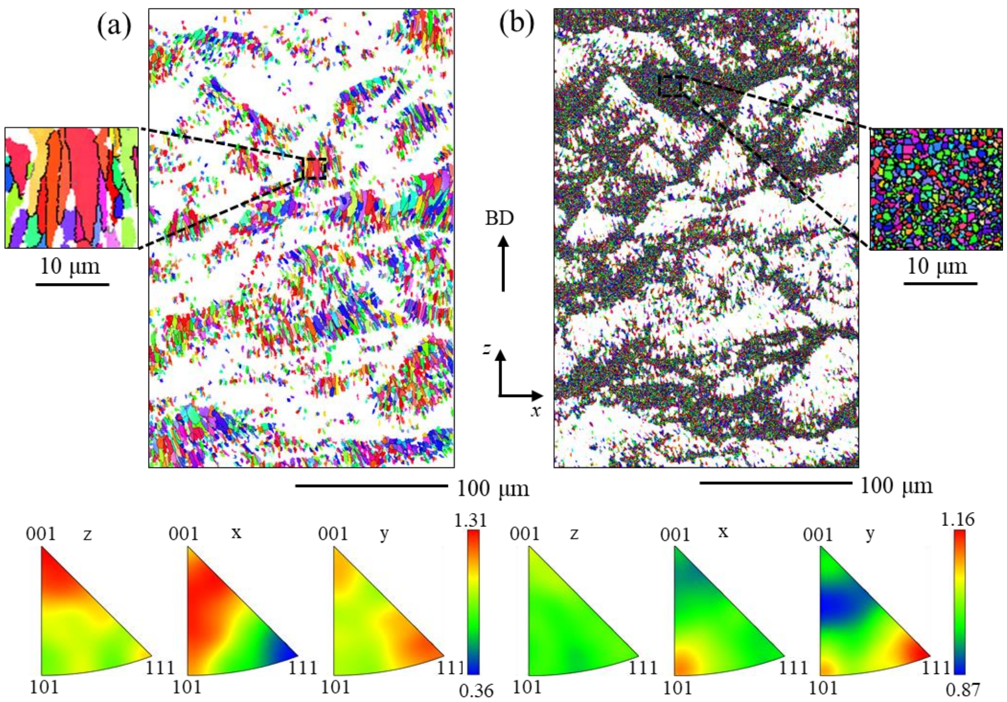

Fig. 5. EBSD data of the as-built sample, grain structure and orientation distribution of the grains larger than 2 μm (a) and the ones smaller than 2 μm (b). BD represents building direction.

3.2 Defect characteristics

In the present work, focus is placed on defects that may notably influence the ductility of LPBF AA7075-Zr. These defects are large secondary particles and pores with a wide range of size. According to the energy dispersion spectrum (EDS), the large secondary particles are rich in Zr in both the AB and HT samples, and their size distribution is almost unchanged after the HT, see Fig. 6a. Given that the pore size has a very large range, the statistics are performed with two sets of SEM images acquired at two different magnifications. Correspondingly, the pores are divided into small pore (1-15 μm) and large pore (>15 μm) groups, as shown in Fig. 6b and c, respectively. The small pores are generally round, possibly resulting from the hydrogen gas emitted from the ZrH_2 particles or from the Mg and Zn vaporization. In contrast, the very large pores generally present irregular shapes. They are generally referred to as lack-of-fusion (LoF) defects. The area fractions of the pore defects (including the small and large ones) are 0.36% and 0.28% for the AB and HT states, respectively.

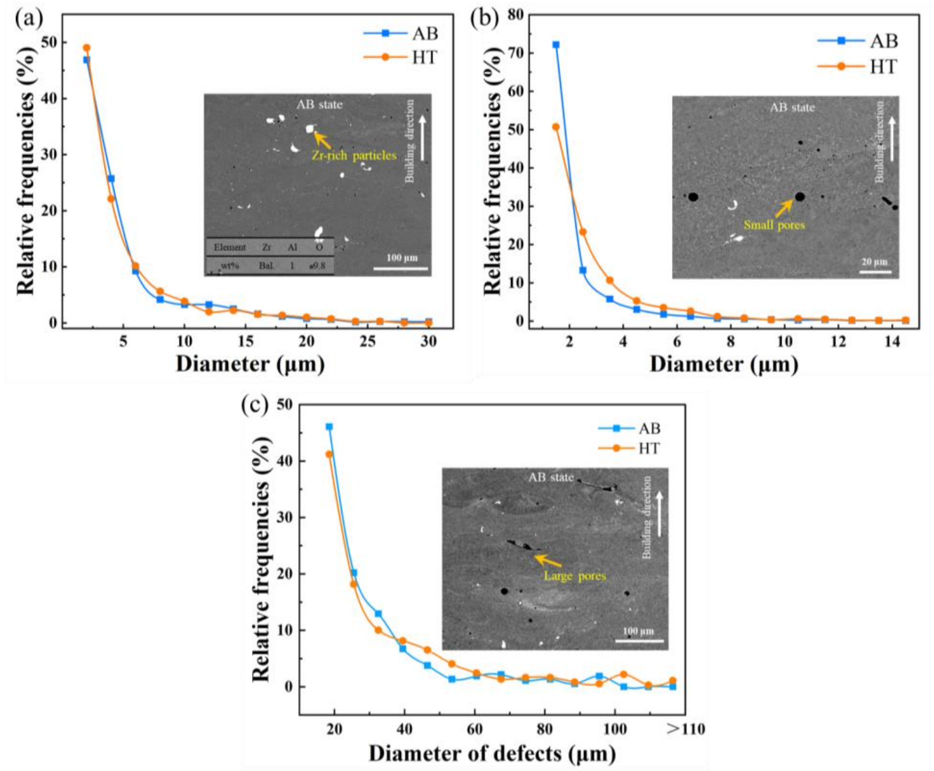

Fig. 6. Size distribution of Zr-rich particles (a), small pores (1-15 μm) (b) and large pores (>15 μm) (c) for the AB and HT states. The defect quantities for statistics for each state are over 1100 for the Zr-rich particles, over 13000 for the small pores and over 370 for the large pores.

From Fig. 6b, it can be seen that the pores smaller than 2 μm are predominant for the AB state, whereas their quantity drops after the HT, implying that the tiny gas pores might be partially "healed" during the HT. For the large pores, their size distribution changes very little before and after the HT, as revealed by Fig. 6c. The healing of small round pores has also been reported in LPBF AA4xxx and was attributed to Mg diffusion [39]. The nano-CT characterization allows to justify the healing phenomenon. Fig. 7a presents the 3D visualization of pores in the same region before and after the heat treatment (425 °C for 1h). It is clearly observed that the majority of submicron (or even nano) pores have been removed by the heat treatment. Quantitatively, pores smaller than 0.5 μm are 94% (number based) healed, pores in the range of 0.5 μm-1 μm are 78% (number based) healed, as shown by Fig. 7b (the error bars correspond to the standard deviations obtained for all the pores analyzed in each diameter interval). Further analysis would be needed to explain the mechanism of healing of these small pores, but it lies outside of the scope of this work.

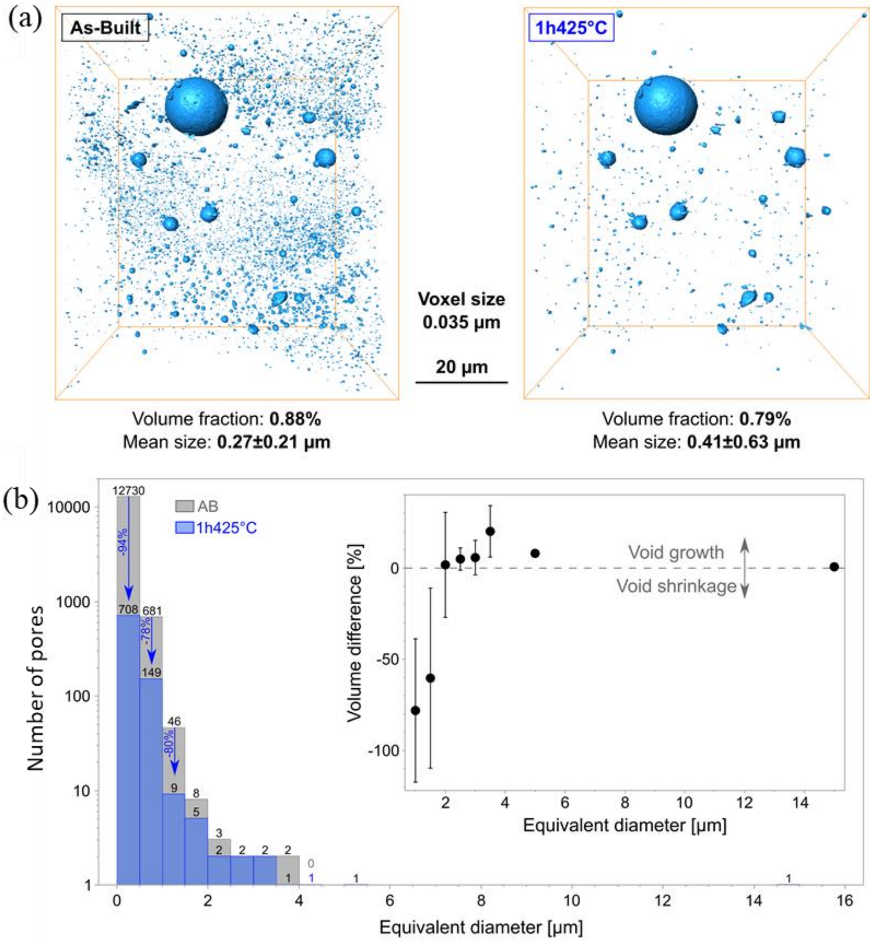

Fig. 7. Nano-CT scan before and after 1h 425 °C HT (a), porosity size distribution for the nano-CT scan (b). The inset of (b) also shows the mean volume difference of the pores larger than 1 μm depending on their size. Note the logarithmic scale for the number of pores.

Interestingly, the inset of Fig. 7b reveals a slight increase in the volume of the pores larger than 2 μm. This implies that these pores tend to grow during the heating, presumably by absorbing the hydrogen released from the healed submicron pores or by increased inner pressure due to heating. Through high resolution SEM characterization, it is found that the submicron or even nano-sized pores are mainly located in the FGZ, as illustrated in Fig. S2 in the supplementary material. This could be due to the fact that the gas released at the melt pool border could possibly be more easily captured by the solidification front.

The long and sharp defects are generally detrimental to the mechanical performance of LPBF alloys [40]. The large defects are carefully examined in the present work. Fig. 8 illustrates their location, orientation and size distribution in the AB samples extracted from the center region of the build. The defects mostly have a length larger than 50 μm. The typical morphologies of the large defects are shown in Fig. 8a and b, for the orientations perpendicular and parallel to the building direction (BD), respectively. The defects perpendicular to the BD are typical lack-of-fusion (LoF) defects (Fig. 8a), whereas the defects parallel to the BD appear to be solidification cracks generated at grain boundaries (Fig. 8b). Most large defects are located in the CGZ or mixing zone (traversing both FGZ and CGZ, e.g. in Fig. 8a), as shown in Fig. 8c. In addition, the quantity of the LoF defects is much higher than that of the solidification cracks, as reflected by the appearance frequencies (number based) of the two orientations of the large defects (see Fig. 8c). The average length of the LoF defects is 95 μm ± 40 μm. The longest detected reaches 220 μm (Fig. 8d). The solidification defects are much shorter, their length being generally below 60 μm, with a mean size of 45 μm and a standard deviation of 10 μm.

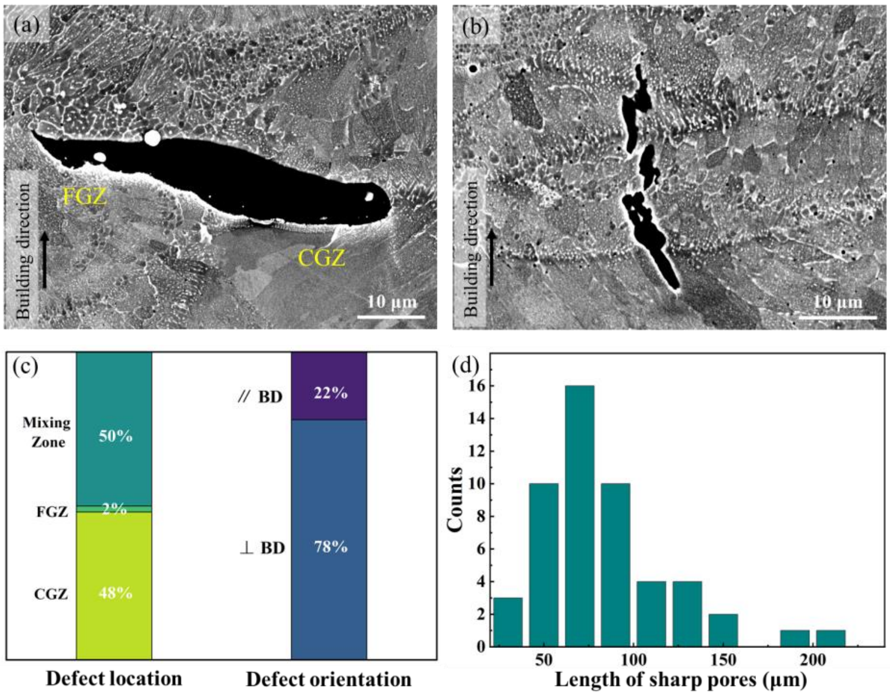

Fig. 8. Typical large/sharp defects perpendicular (a) and parallel (b) to the building direction, preference of location and orientation (c) as well as length distribution of these large defects (d). There are 50 defects extracted for statistical analysis in total.

3.3 Mechanical properties

The macroscopic stress-strain curves for the two material states (i.e. AB and HT) and the two loading directions (i.e. horizontal and vertical) are presented in Fig. 9. The strain values are obtained from the macroscale DIC measurements. For a given DIC strain field, the central region of 0.8×0.8 mm (see the insets in Fig. 9) is extracted to calculate the average strain, which is then employed to plot the stress-strain curves. The curves marked as "Break" correspond to tensile tests to failure, so the ductility can be assessed. The ones marked as "Interrupted" refer to tensile tests terminated before failure, they serve to assess the damage behavior of the LPBF AA7075-Zr in different states and loaded along different directions. It is noteworthy that the flow stress slightly drops after yielding, especially for the HT state (see Fig. 9b). This phenomenon is frequently observed in LPBF AA7075 alloy incorporating heterogeneous nucleants [12, 14, 22, 27], and could be due to the dynamic strain ageing effect [14].

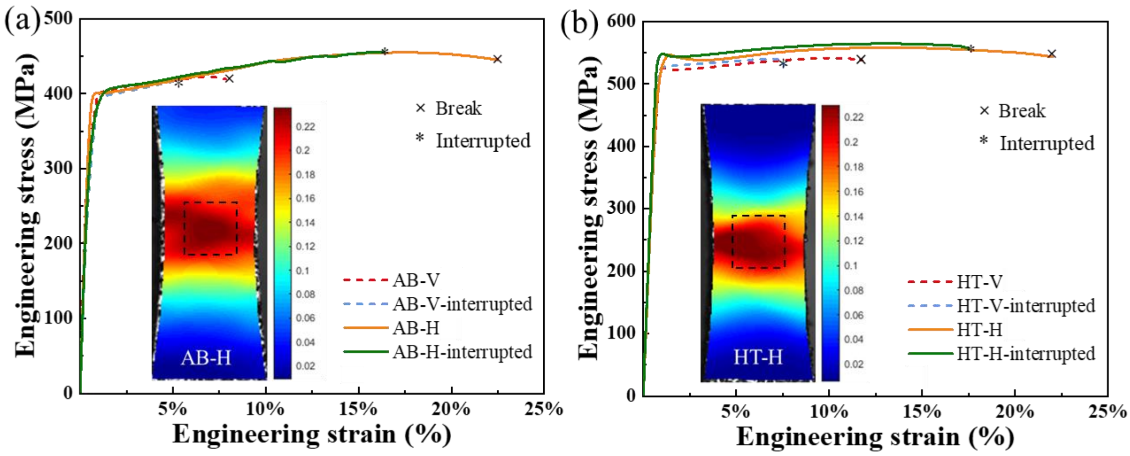

Fig. 9. Macroscopic tensile engineering stress-strain curves of LPBF AA7075-Zr for the as-built (a) and heat treated (b) states.

The yield strength and strain at fracture are presented in Table 3. It is found that the HT significantly improves the yield strength in both the horizontal and vertical directions. The horizontal samples present a slightly higher strength than the vertical counterparts, especially after the HT, but the strength anisotropy is weak. Moreover, the horizontal samples exhibit a much higher ductility compared to the vertical ones for both the AB and HT states. Moreover, the T6 heat treatment (HT) does not significantly change their respective ductility. The tensile properties obtained with standard samples in the horizontal direction are as follow [30]: the yield strength and true strain at fracture ($\ln(A_0/A_f)$, with A_0 and A_f representing the cross-section area prior to loading and after fracture, respectively) are 380 ± 9 MPa and 18% ± 3% for the AB state, while they are 515 ± 7 MPa and 21% ± 3% for the HT state, respectively. The slightly higher yield strength for the small samples is due to the R15 notch (Fig. 2b) that induces a traverse stress and hence a triaxial stress state [41, 42]. The strain at fracture is close between the small and standard tensile samples, for both the AB and HT states. Therefore, the utilization of small samples for obtaining macroscopic tensile properties can be considered valid.

Table 3. Yield strength and strain at fracture of LPBF AA7075-Zr in different states and loaded along different directions. These properties are determined from small, non-standard tensile tests specimens.

Sample state	Loading direction	Yield strength (MPa)	Strain at fracture (%)
AB	Vertical	403 ± 4	8.2 ± 2.0
	Horizontal	406 ± 5	21.2 ± 1.6
HT	Vertical	528 ± 7	10.5 ± 0.5
	Horizontal	553 ± 7	20.8 ± 1.9

3.4 Local strain distribution

The microscale (grain-scale) strain distribution is correlated to the microstructure heterogeneity within melt pools. Nanoindentation tests allow to probe the microstructure controlled local strength, as shown in Fig. 10 and Table 4. Fig. 10d shows the hardness distributions for both the AB and HT states. It is found that the heat treatment significantly enhances the hardness (from 1.81 GPa to 2.28 GPa), in line with the yield strengths obtained by the tensile tests (Table 3). For the AB state, the hardness exhibits a clear correlation with the grain size (Fig. 10b and e), the average hardness being higher in the FGZ (1.88 GPa vs. 1.73 GPa, see Table 4). However, the correlation between the hardness and the melt pool structure is significantly weakened after the heat treatment (Fig. 10c and f). Although there exist few coarse grains presenting low hardness (see Fig. 10c), the average hardness values are nearly the same for the CGZ and FGZ (2.29 GPa vs. 2.26 GPa, see Table 4). These results indicate that the T6 heat treatment homogenizes the microstructure and consequently the local mechanical properties of the LPBF AA7075-Zr samples. The similar strength between the FGZ and CGZ of the HT sample could be explained by the more significant precipitate strengthening in the CGZ that compensates the Hall-Petch effect favoring a higher strength for the FGZ [30].

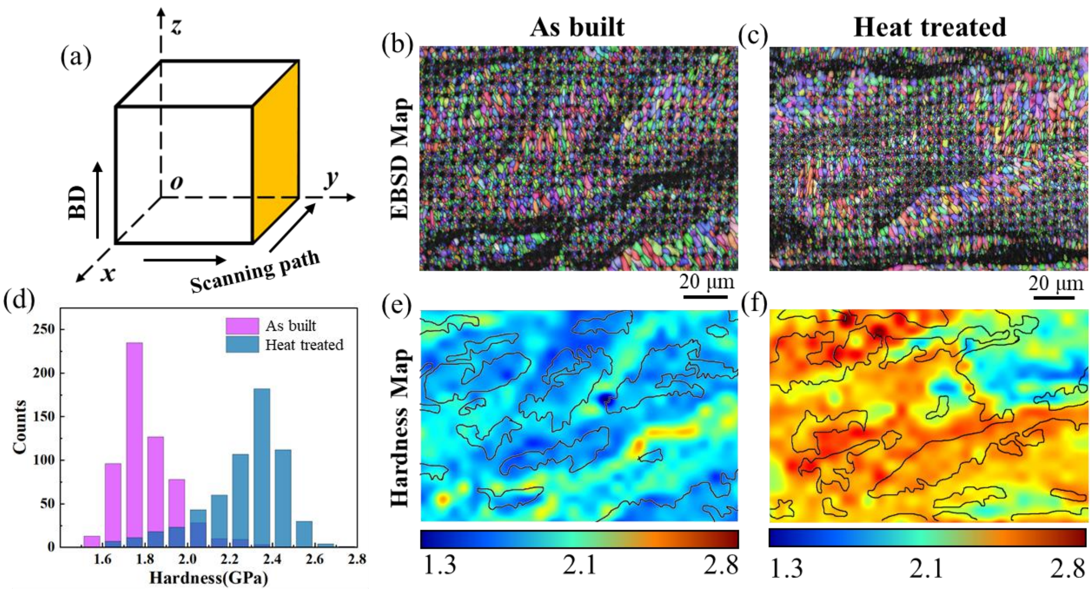

Fig. 10. Nanoindentation measurements of LPBF AA7075-Zr. The cross section for the indentation tests (a), the indent matrix overlapped with EBSD map for the as-built (b) and heat treated samples (c), hardness distributions (d), hardness maps for the as-built (e) and heat treated (f) states. The black lines in (e) and (f) enclose the CGZ.

Table 4. Mean hardness values measured by nanoindentation.

Sample state	Averaged hardness (GPa)	Hardness of CGZ (GPa)	Hardness of FGZ (GPa)
As-built	1.81 ± 0.14	1.73 ± 0.08	1.88 ± 0.14
Heat treated	2.28 ± 0.19	2.29 ± 0.19	2.26 ± 0.2

The in-situ SEM tensile tests aided by the HR-DIC measurement allow to quantitatively assess the microscale strain distribution and understand the deformation mechanisms for the considered two material states (AB and HT) and the two loading directions (H and V). It is noteworthy that the strain fields were calculated in the Lagrangian configuration (i.e. initial configuration), so that they can be superposed on the microstructure acquired prior to loading. The strain component in the loading direction is presented in the rest of the paper, which is also the maximum principal strain in the uniaxial tensile loading scenario. Fig. 11 shows the strain fields of the AB-V sample with increasing global deformation level, with individual color scale for each strain map. Note that if the color scale is unified, the strain inhomogeneity cannot be clearly revealed when the global strain is relatively low, as illustrated in Fig. S3 in the supplementary material. From Fig. 11, it can be clearly seen that the strain field is highly inhomogeneous, with some regions presenting notable strain concentration (in red) and some regions presenting much lower strain (in blue) than the average strain. Moreover, the strain localization behavior seems to maintain during the deformation of the whole sample.

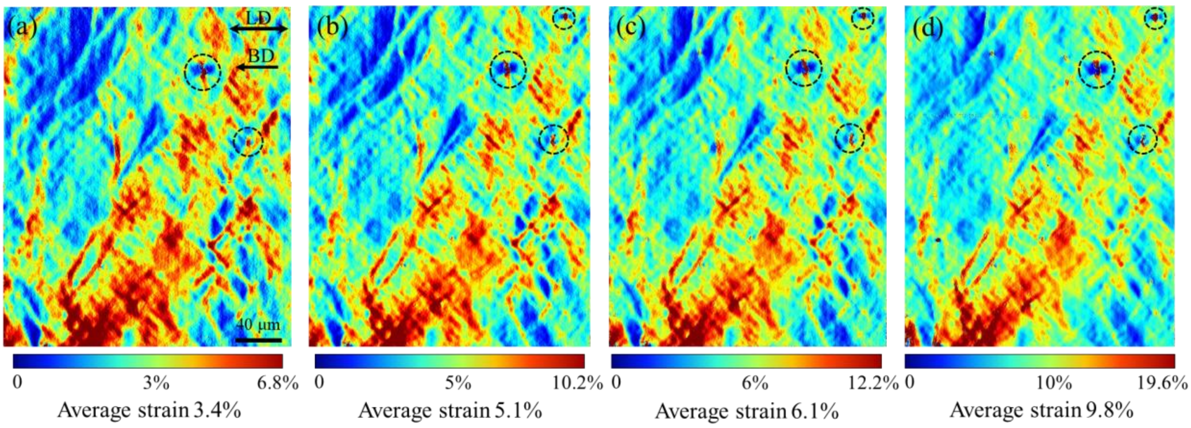

Fig. 11. In-situ HR-DIC results (xz-plane) of the strain component in the loading direction for the AB-V sample at the average strain of 3.4% (a), 5.1% (b), 6.1% (c) and 9.8% (d). The dashed circles in (a) highlight the pre-existing pores. LD and BD represent loading direction and building direction, respectively.

The aforementioned non-homogeneous strain field is expected to be related with the heterogeneous microstructure of LPBF AA7075-Zr. Fig. 12 shows an overlapping of microstructure morphology and strain map for the AB-V sample deforming to ε_{avg}=5.1%. A relatively clear correlation between the strain field and the melt pool structure is found. In general, the CGZ and specific bands are the locations of strain concentration (Fig. 12b and c), whereas the FGZ generally present lower strain (Fig. 12d). This is consistent with the higher (respectively lower) hardness of the FGZ (respectively CGZ) previously shown in Fig. 10.

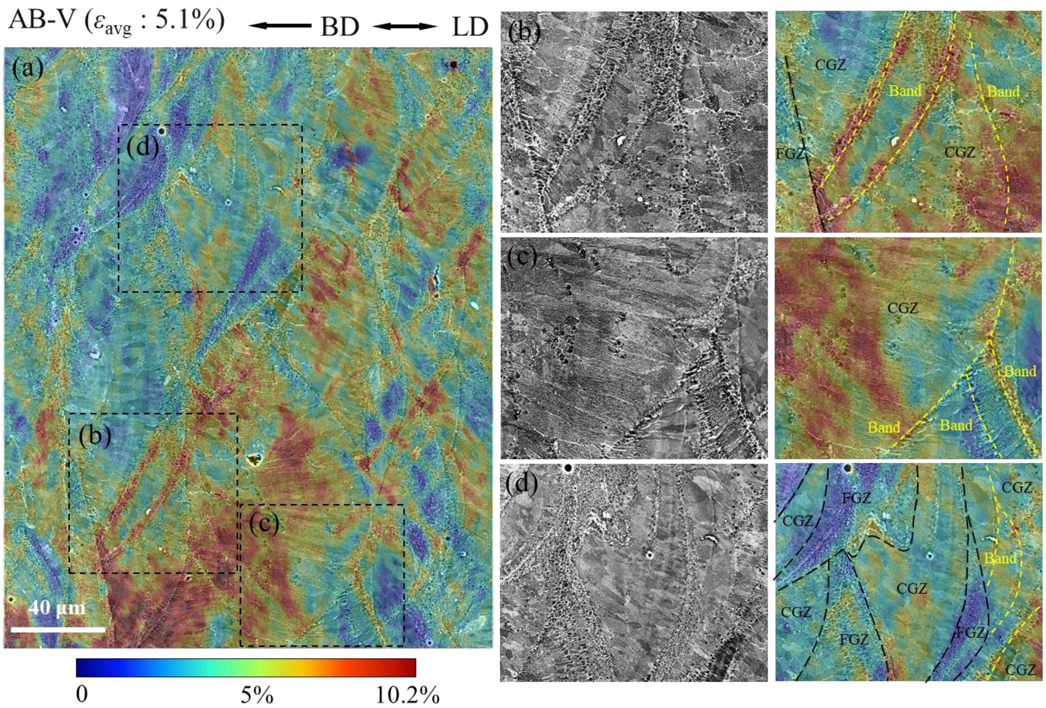

Fig. 12. Overlapped strain map with microstructure for the AB-V sample. Overall strain fields in the region of interest (a), local strain fields and their correlations with the microstructure (b), (c) and (d). BD and LD represent building direction and loading direction, respectively.

The strain field evolution with the global deformation of the AB-H sample is presented in Fig. 13. Similarly to the AB-V sample, the strain field is also highly inhomogeneous for the

AB-H counterpart, where some regions present much higher or lower strain than the average strain of the whole map. In addition, there seem to be some deformation bands forming 45° with the loading direction, as will further be highlighted in Fig. 14. Such deformation bands are not observed for the AB-V sample.

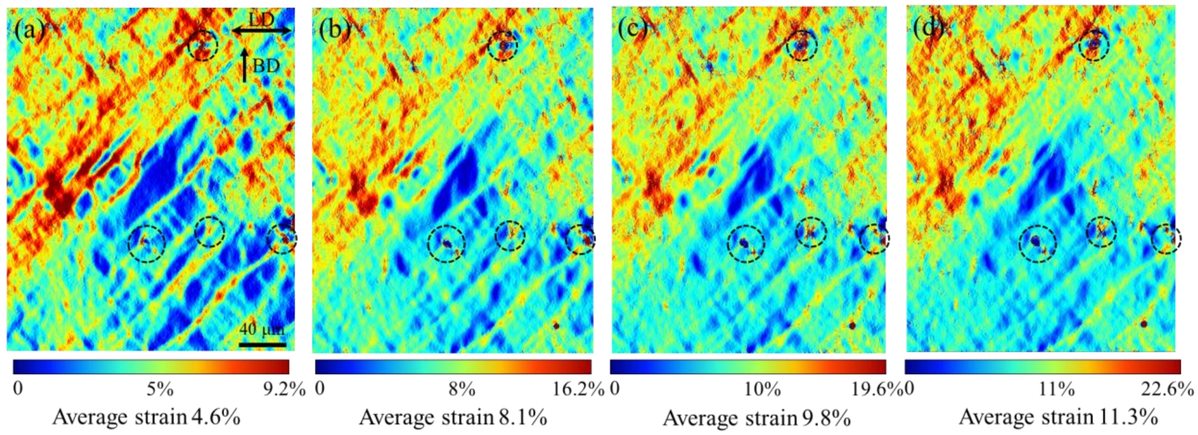

Fig. 13. In-situ HR-DIC results (xz-plane) of the strain component in the loading direction for the AB-H sample at the average strain of 4.6% (a), 8.1% (b), 9.8% (c) and 11.3% (d). The dashed circles in (a) highlight the pre-existing pores. LD and BD represent loading direction and building direction, respectively.

A similar microstructure-strain field correlation as for the AB-V sample is observed for the AB-H case, as shown by the overlapped strain map (ε_{avg}=4.6%) with the microstructure in Fig. 14. The strain concentration generally occurs in the CGZ and specific bands (Fig. 14b and c), which is consistent with the lower hardness of the CGZ. In particular, the strain bands orientating at 45° with respect to the loading direction (LD) are mainly located in certain large FGZ (highlighted by the blue dotted lines in Fig. 14d), this can be related to the largest shear stress in the uniaxial loading scenario that provides a sufficient driving force for the plastic deformation of the large FGZ. Note that the FGZ presents random grain orientations, as previously shown in Fig. 5.

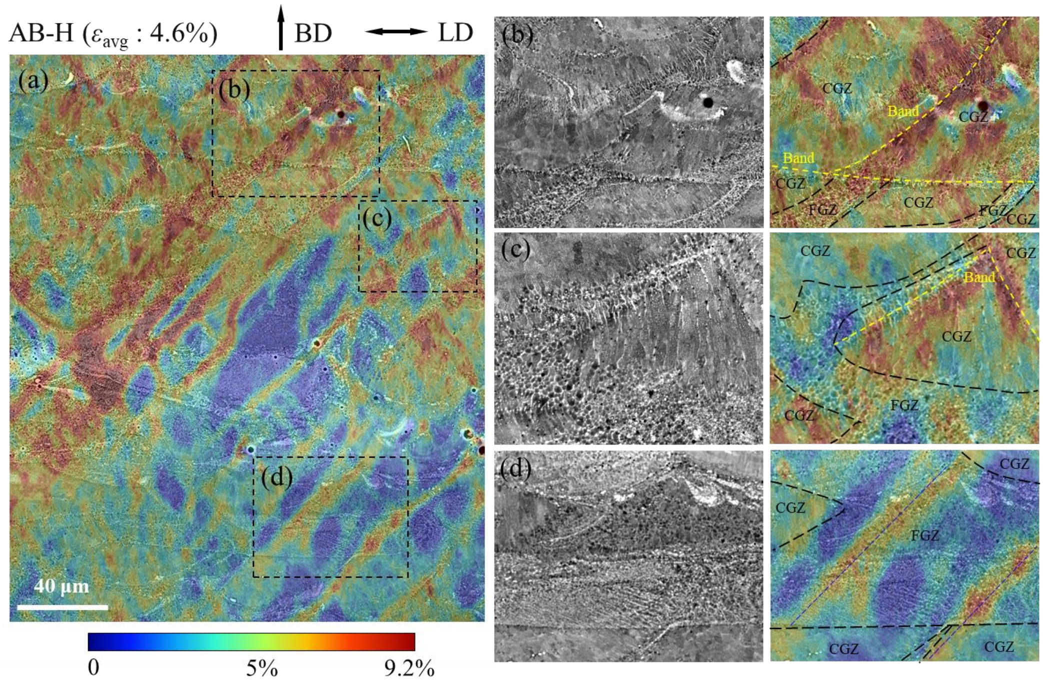

Fig. 14. Overlapped strain map with microstructure for the AB-H sample. Overall strain fields in the region of interest (a), local strain fields and their correlations with the microstructure (b), (c) and (d). LD and BD represent loading direction and building direction, respectively.

Concerning the heat treated samples, the average hardness is found to be very close between the CGZ and FGZ (Table 4), with some large columnar grains presenting lower hardness (see Fig. 10c and f). Correspondingly, the correlation between melt pool structure and microscale strain field is expected to be weakened. Fig. 15 illustrates the evolution of strain fields as a function of the global deformation level of the HT-V sample. The strain distribution appears to be less inhomogeneous compared to the two AB samples, as will be quantitatively revealed in Fig. 19. Nevertheless, besides strain localization induced by the pre-existing pores (see the dashed circles in Fig. 15a), there are still some regions experiencing strain concentration, as can be seen in the bottom right corner of the strain map.

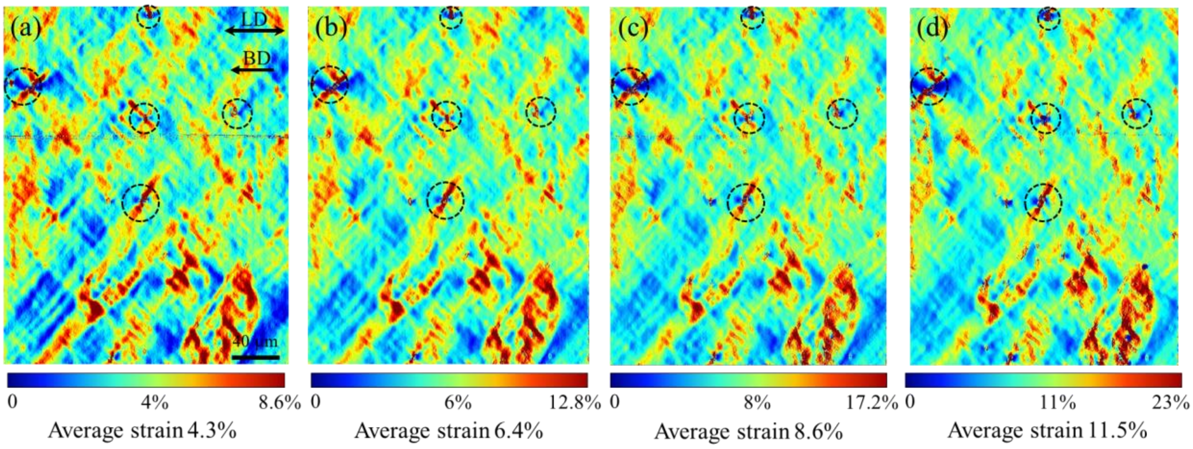

Fig. 15. In-situ HR-DIC results (xz-plane) of the strain component in the loading direction for the HT-V sample at the average strain of 4.3% (a), 6.4% (b), 8.6% (c) and 11.5% (d). The dashed circles in (a) highlight the pre-existing pores. LD and BD represent loading direction and building direction, respectively.

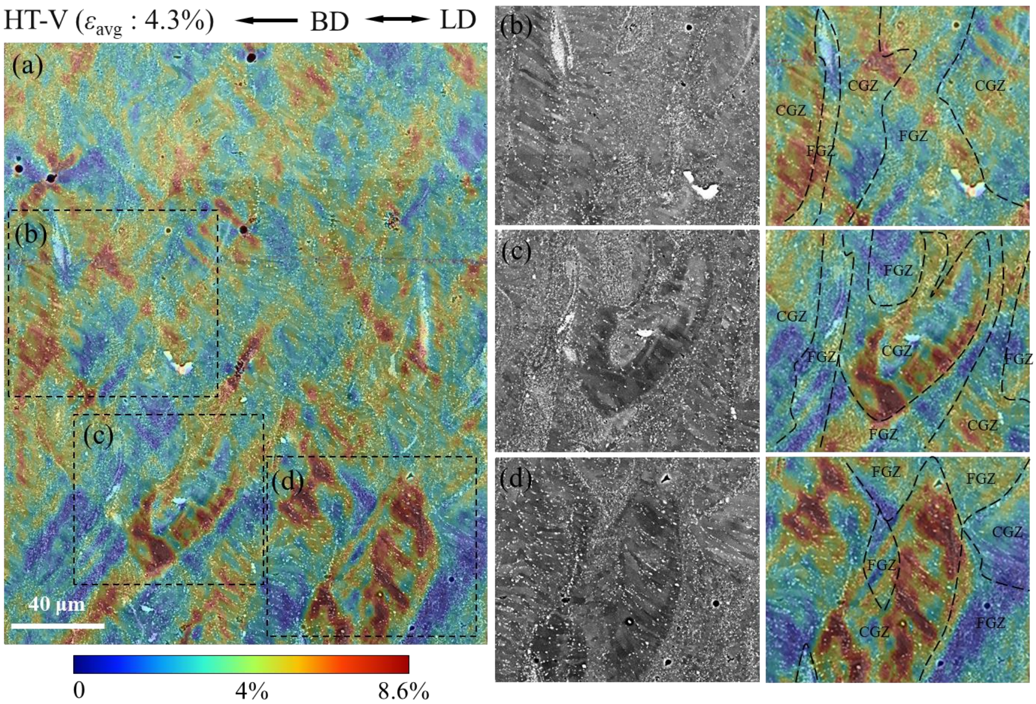

Fig. 16. Overlapped strain map with microstructure for the HT-V sample. Overall strain fields in the region

of interest (a), local strain fields and their correlations with the microstructure (b), (c) and (d). LD and BD represent loading direction and building direction, respectively.

The overlapped strain map (ε_{avg}=4.3%) with the microstructure clearly demonstrates that the aforementioned strain concentration regions are the CGZ, as shown in Fig. 16b, c and d. It is noteworthy that only part of columnar grains present the pronounced strain concentration in the relatively large CGZ (see Fig. 16d), in contrast to the AB-V sample where a large fraction of CGZ experiences strain concentration (see Fig. 12).

The HT-H sample shows a relatively more homogeneous strain distribution, as can be observed in Fig. 17. The strain field is much more homogeneous than that of the AB-V, AB-H and HT-V samples. This will be further shown in Fig. 19. Excluding the influence of the pre-existing pores (see the dashed circles in Fig. 17a), there are only very slight deformation concentration bands, mostly forming an angle of 45° with the loading direction. Moreover, the strain concentration degree in these deformation bands appears to further reduce during the global deformation of the sample.

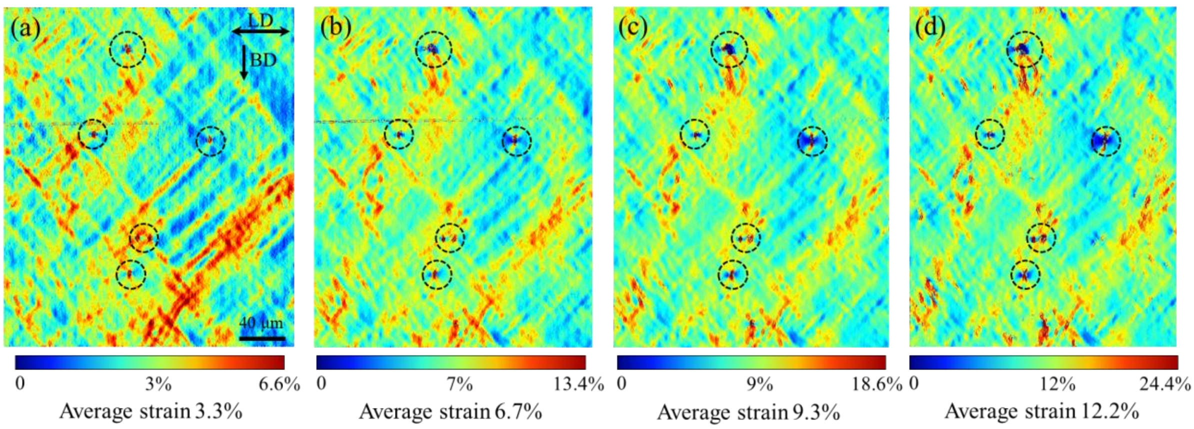

Fig. 17. In-situ HR-DIC results (xz-plane) of the strain component in the loading direction for the HT-H sample at the average strain of 3.3% (a), 6.7% (b), 9.3% (c) and 12.2% (d). The dashed circles in (a)

highlight the pre-existing pores. LD and BD represent loading direction and building direction, respectively.

Fig. 18 shows the overlapped strain field (ε_{avg}=6.7%) with the microstructure of the HT-H sample. It can be seen that there is no clear correlation between the strain field and the microstructure. The observed slight strain concentration could be induced by a grain orientation effect. For the FCC metals, the <001> orientation leads to the lowest strength while the <111> orientation leads to the highest strength [43].

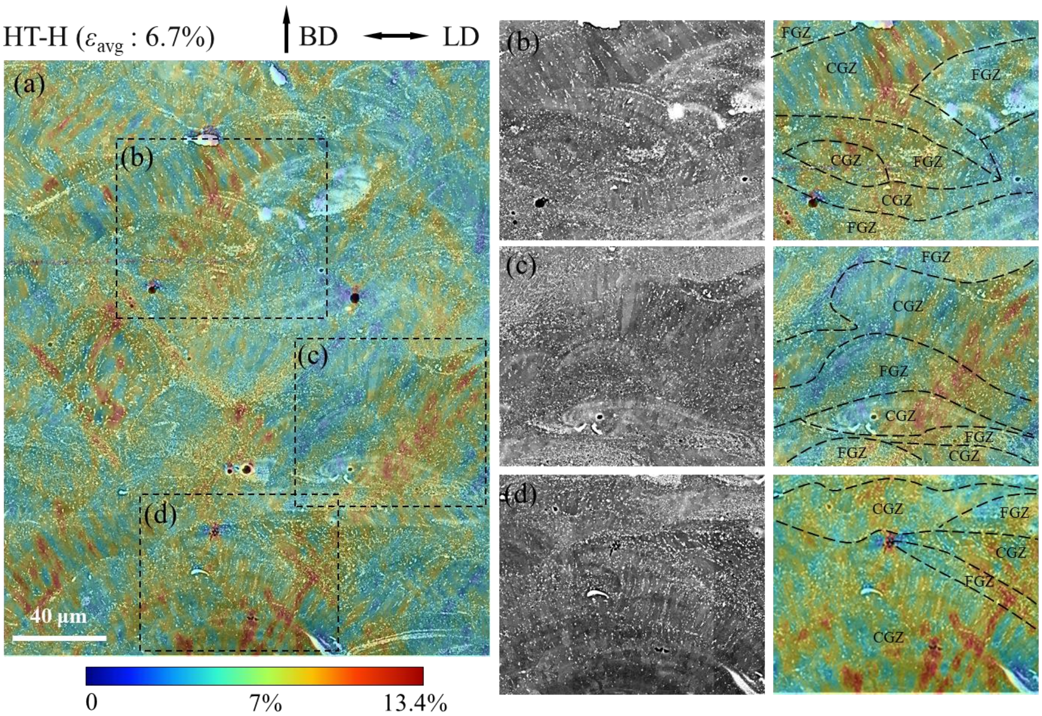

Fig. 18. Overlapped strain map with microstructure for the HT-H sample. Overall strain fields in the region of interest (a), local strain fields and their correlations to the microstructure (b), (c) and (d). LD and BD represent loading direction and building direction, respectively.

To quantitatively reveal the strain inhomogeneities in the AB-V, AB-H, HT-V and HT-H samples, area-weighted strain distributions are plotted in Fig. 19. A wider distribution curve corresponds to a more inhomogeneous strain distribution. It can be seen that the two AB samples present a similar strain distribution, while the two HT samples exhibit a narrower distribution, especially for the HT-H sample. This indicates a more homogeneous strain distribution after the HT homogenizes the melt pool microstructure.

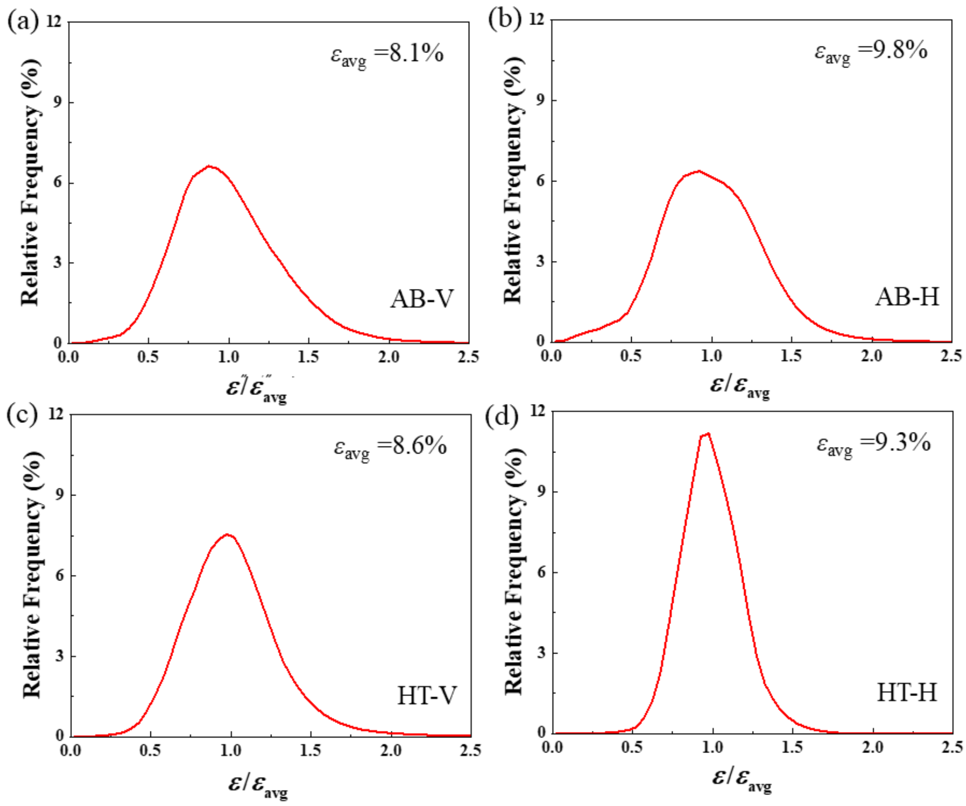

Fig. 19. Area-weighted strain distribution for the AB-V (a), AB-H (b), HT-V (c) and HT-H (d) samples.

To further assess the correlation between the local strain and the heterogeneous melt pool microstructure, the average strain values for different melt pool regions are extracted and plotted in Fig. 20. It can be seen that the strain inhomogeneity is quite significant for the AB state, the specific microstructure bands accommodating the highest strain and the FGZ the lowest strain (Fig. 20a and b). It is noteworthy that the specific microstructure bands disappear upon the HT, as previously shown in Fig. 4b. Regarding the HT-V sample, the CGZ still presents a higher average strain compared to the FGZ, but the difference between the regions is reduced with respect to the AB-V sample (Fig. 20c). As for the HT-H sample, the average strain is nearly the same in the CGZ and FGZ (Fig. 20d), indicating a negligible correlation between the strain concentration and the underlying melt pool microstructure.

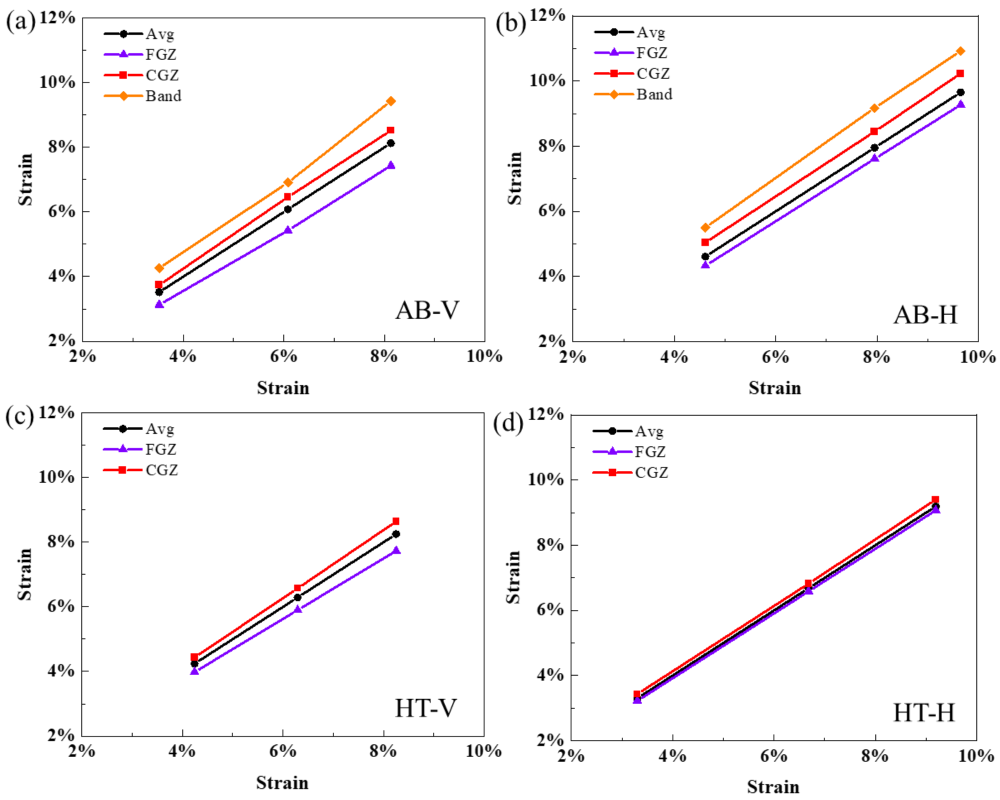

Fig. 20. Evolution of average strain levels in different regions for the AB-V (a), AB-H (b), HT-V (c) and HT-H (d) samples.

3.5 Damage and fracture

To reveal the damage behavior and understand the origin of ductility anisotropy, both the broken samples and interrupted tensile samples are examined. Fig. 21 illustrates the typical fracture surface morphologies of the AB-V, AB-H, HT-V and HT-H samples. For the vertical loading direction, large LoF defects are observed (Fig. 21a1, a2, c1, c2), implying that they play a vital role in the failure of the sample. For the horizontal loading direction, sharp and large pores are eventually found on the fracture surface, but they are not in a favorable orientation promoting the fracture of the sample (Fig. 21b1, b2, d1). In contrast, massive gas pores of different sizes can be seen, and the pore density is significantly higher than that for the vertical loading direction. This indicates that the round gas pores contribute significantly to the damage and fracture of the samples, especially for the horizontal loading direction.

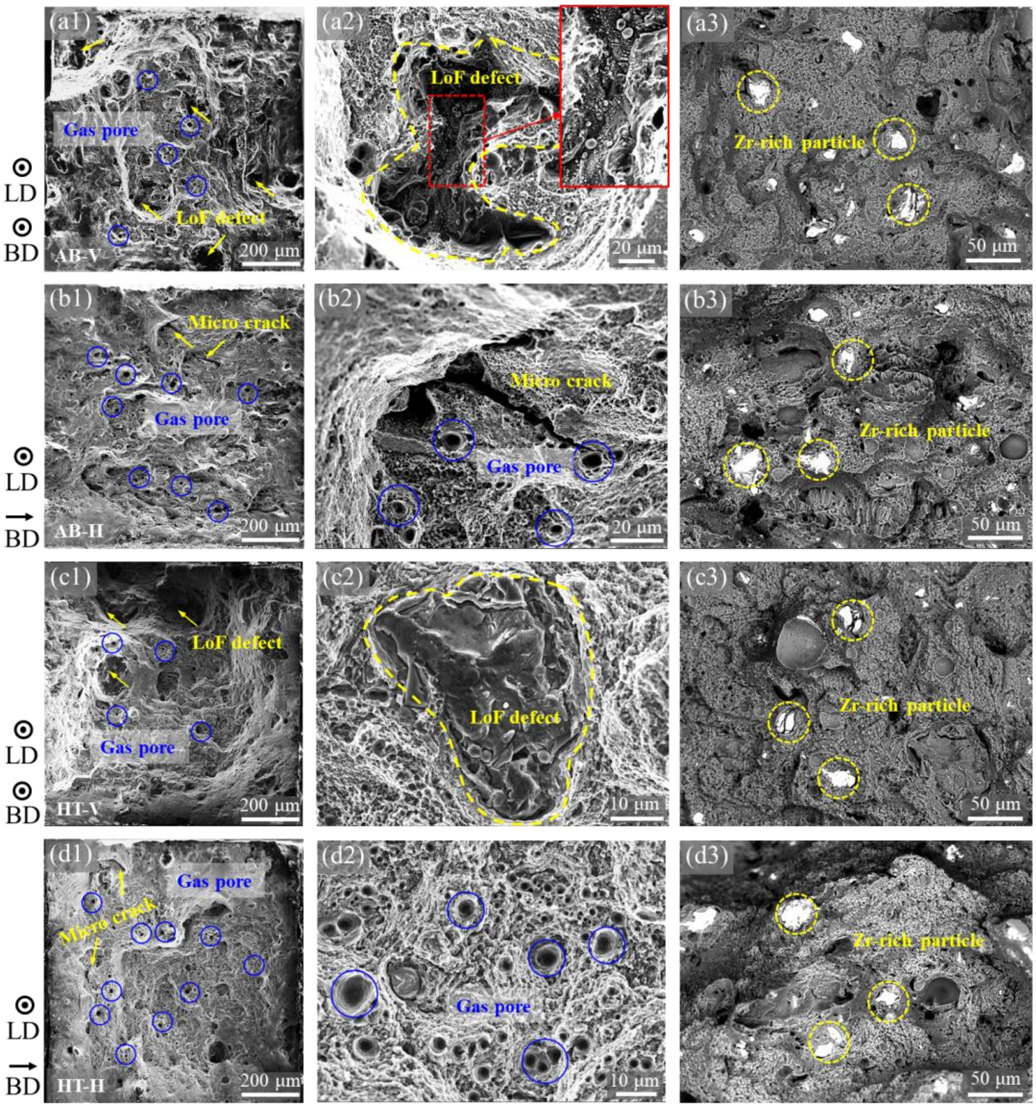

Fig. 21. Fracture surface morphologies for the AB-V (a1)-(a3), AB-H (b1)-(b3), HT-V (c1)-(c3) and HT-H (d1)-(d3) samples. LD and BD represent loading direction and building direction, respectively.

In addition to the pores, large Zr-rich particles are also observed for the four cases, as illustrated by Fig. 21a3-d3. This means that these secondary phases are also potential damage sites triggering the main crack or coalescing to the main crack tip.

High magnification SEM images are acquired to reveal the dimple features, which allow to assess the secondary damage events between the large pores or the voids generated by Zr-rich particle fracture. Fig. 22 shows the typical dimple morphologies for the four cases, with the scale bar being identical for a clear comparison. From Fig. 22a and b, it can be seen that the dimples contain very small particles for the AB samples. These particles could be the $L1_2$ Al_3Zr in the FGZ, the precipitates within the CGZ or the continuous network enclosing the grains [30]. As for the HT-V sample, the dimples appear to be larger than those for the AB samples, and the particles in the dimples are also much bigger (see Fig. 22c). Instead of being round, some of the dimples of the HT-H sample present irregular shapes. Such feature is reminiscent of the mixture of intergranular and intragranular cracking [44].

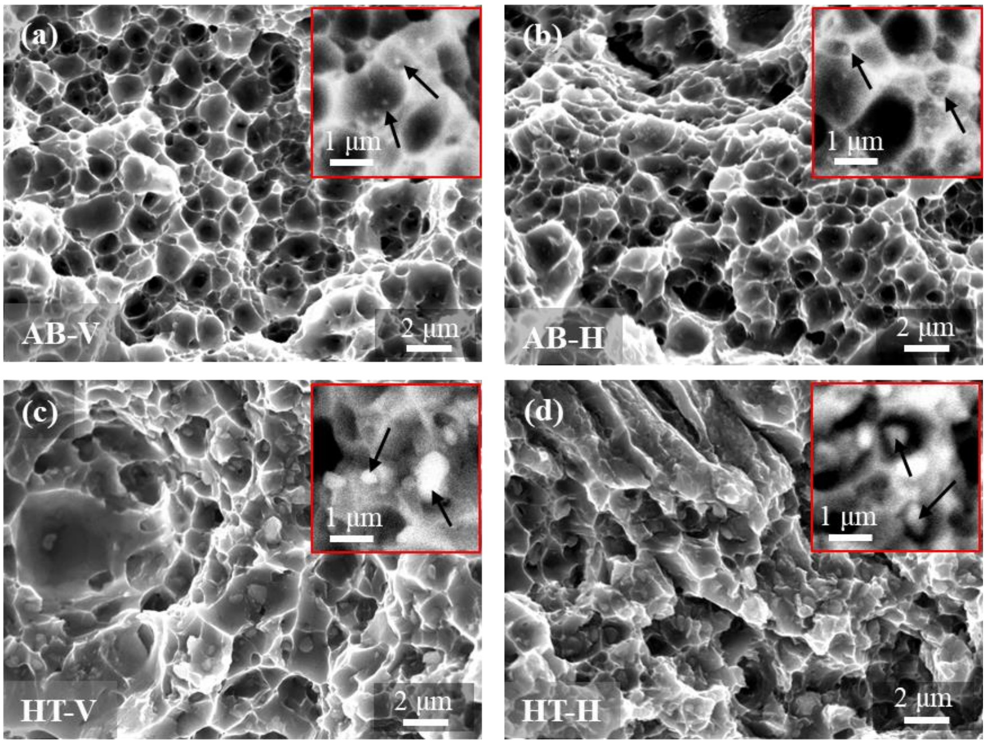

Fig. 22. High magnification SEM images showing the dimple features of the AB-V (a), AB-H (b), HT-V (c) and HT-H (d) samples, respectively. The insets are acquired under the backscatter mode to enhance the contrast of the particles.

The fracture surface morphologies only disclose the final state of failure. To better understand the damage behavior, the samples recovered from the interrupted tensile tests are carefully analyzed. Fig. 23 illustrates the damage features observed at the mid-thickness plane (i.e. polished to mid-thickness plane) for the AB-V, AB-H, HT-V and HT-H samples, bringing to light the following observations:

(i) For the vertical loading direction, the preexisting large/sharp pores extend and eventually coalesce with newly formed pores/micro-cracks, as can be seen in Fig. 23a1, c1, c2 and c3.

(ii) For the horizontal loading direction, the initial large/sharp pores barely propagate as they are nearly parallel to the applied load, as revealed by Fig. 23b3 and d2.

(iii) For the AB state, the dense gas pores in the FGZ (Fig. 7a) eventually grow and coalesce to larger pores (Fig. 23b2) or even micro-cracks (Fig. 23a2). Moreover, the specific bands experiencing severe strain concentration may produce voids which coalesce with preexisting pores, as can be seen in Fig. 23a3 and b4. These two damage mechanisms are not present in the HT samples due to less pores (Fig. 7b) and the absence of the specific microstructure bands (Fig. 4b).

(iv) For the HT state, as the flow stress is much higher than that in the AB state, two additional damage mechanisms emerge, one is the tearing of preexisting gas pores (Fig. 23c4), which might be assisted by the remaining tiny pores (although partially healed by the HT, see Fig. 7b); the other is the cracking of Zr-rich particles, which is more frequently observed in the horizontal loading case (Fig. 23d1). This is due to the fact that the horizontal sample is much more deformed before interruption, as it can withstand higher loads (see Fig. 9b).

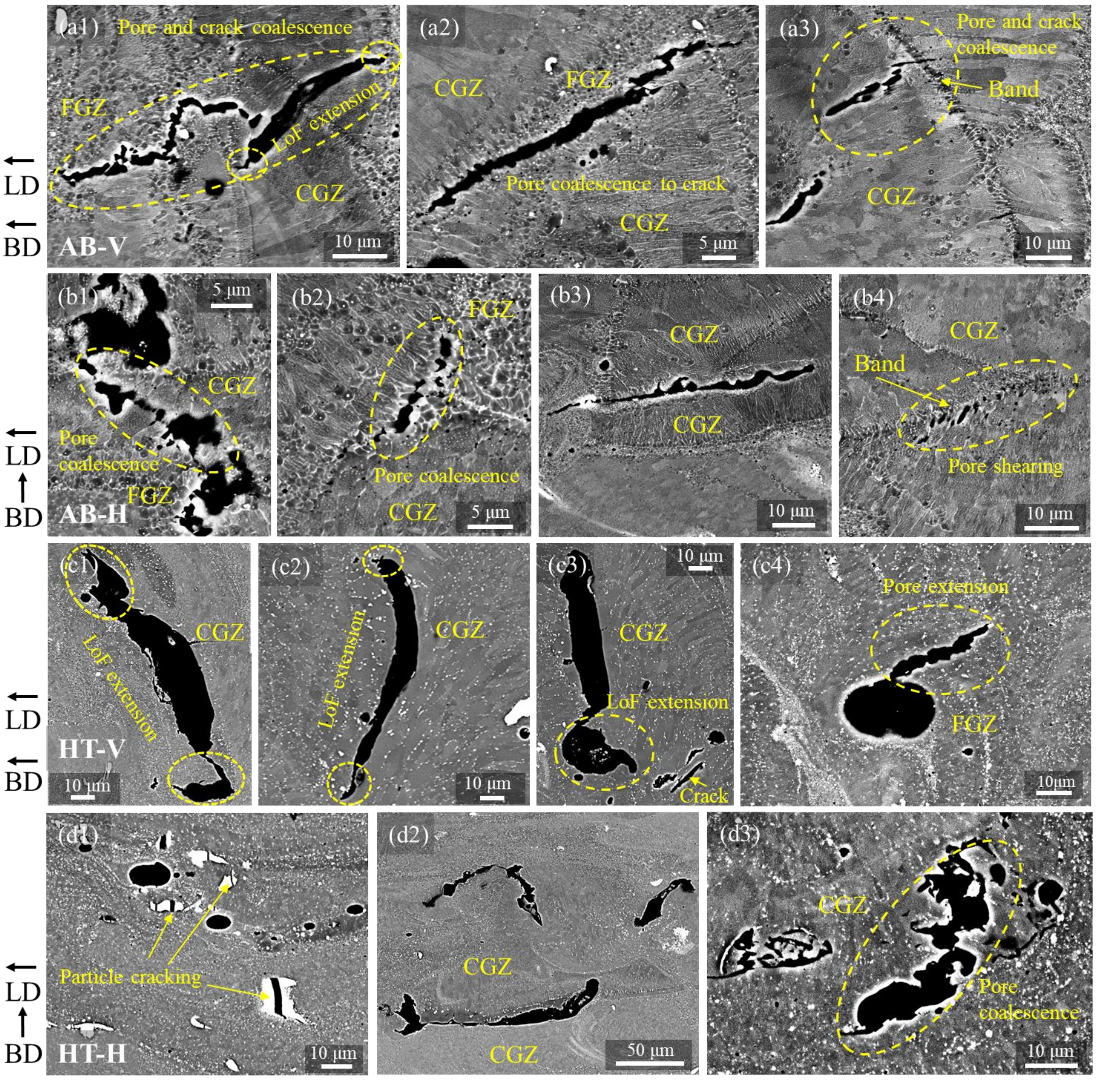

Fig. 23. Damage observations at mid-thickness planes of interrupted tensile samples. AB-V sample deformed to 5.6% (a1)-(a3), AB-H sample deformed to 16.4% (b1)-(b4), HT-V sample deformed to 7.8% (c1)-(c4), HT-H sample deformed to 17.6% (d1)-(d3). LD and BD represent loading direction and building direction, respectively.

4. Discussion

First of all, it is noteworthy that some important discussions about the Zr-modified AA7075 alloy of interest of this work were already conducted in our previous works [29, 30].

It was shown that ZrH_2 successfully suppressed hot cracking for Zr-modified AA7075. Moreover, it was demonstrated that the additional amount of H introduced in the alloy by ZrH_2 did not prevent to reach a 99.9% relative density for the processed samples [29]. Moreover, the specific HT composed of a solid solution at 425 °C for 1h and an artificial aging at 120 °C for 24h was shown to optimize the mechanical properties of the sample. Similar yield strength as wrought AA7075-T6 (see Table 1) has been reached due to the controlled precipitation of nanometric Al_3Zr $L1_2$ hardening precipitates [30].

4.1 Tensile properties

The present work adopts small non-standard tensile samples to investigate deformation mechanisms and mechanical anisotropy of the LPBF AA7075-Zr samples, which are rarely reported in literature. The tensile properties obtained with standard samples in the horizontal direction for both the AB and HT states are given in our related work [30], as also recalled in section 3.3. Note that the elongation to fracture measured with extensometer is 10.1% ± 2.3% and 11.6% ± 0.5% under the AB and HT states, respectively. These properties are better than those reported in the pioneer work solving the hot cracking issue of LPBF AA7075 [12], as can be seen in Table 1. The difference can be explained by the tailored low temperature solution HT that allows to better control Al_3Zr $L1_2$ hardening precipitation than classical higher temperature solution HT at 470°C [30].

When comparing with the works adopting other nucleants (Table 1), the mechanical properties of our samples are above-average. The difference between literature works and the present study are as follows: first, the chemical composition of the AA7075 varies from one work to another, especially in terms of Zn and Mg contents; second, the nature and amount of nucleation agent are not the same, leading to different grain structures; third, different process parameters are adopted in different works, resulting in different element (i.e. Mg and Zn) losses; fourth, the use of a tailored 1h 425°C solution HT improves the efficiency of Zr hardening precipitation [30]. In the present work, a quite significant loss in Mg and Zn has been identified, as shown in Table 2. In future works, such issue can be remedied by adding Mg and Zn to the mixed powder (i.e. AA7075 and ZrH_2) to enhance the mechanical strength of the printed sample for the T6 state.

4.2 Strain concentration

The heterogeneous microstructure of the LPBF AA7075-Zr sample imparts the material distinct mechanical properties of the FGZ and CGZ in the as-built state, which in turn lead to inhomogeneous strain distributions. The CGZ is found to present a lower hardness (Table 4) and correspondingly a higher local strain (Fig. 20) upon deformation during a tensile test. In fact, strain inhomogeneity induced by melt pool microstructure heterogeneity is a common phenomenon for additively manufactured alloys. For example, Song et al. [45] recently showed a notable strain localization at softer melt pool borders of LPBF AlSi10Mg alloy when loaded in the building direction.

The T6 heat treatment allows to homogenize the microstructure, therefore resulting in similar hardness of the FGZ and CGZ in the HT AA 7075-Zr (Table 4). This similar hardness can be explained by two factors. Firstly, the grain size is nearly unchanged after the T6 heat treatment as shown in our previous study [30]. Therefore, according to the Hall-Petch effect, hardness should be larger for the FCG. Secondly, there is more Zr available in solid solution to form Al_3Zr $L1_2$ hardening precipitates inside the CGZ during HT. As a result, a higher volume fraction of these precipitates is present in the CGZ compared to the FGZ (1.6% volume fraction for the CGZ compared to 0.8% for the FGZ), as observed by transmission electron microscopy in our previous study [30]. Accordingly, the CGZ exhibit a higher strengthening by precipitation than the FGZ. This larger precipitation hardening of the CGZ counterbalances the lower Hall-Petch strengthening, explaining the homogeneous hardness observed in Table 4. Correspondingly, the strain inhomogeneity in the HT samples is found to be mitigated compared to the AB samples (Fig. 20). The homogenization of the micro-scale strain distribution by heat treatment has also been reported in a LPBF Al-Si alloy [46].

For both the AB and HT states, the strain inhomogeneity, in particular the strain concentration in the CGZ, appears to be more severe in the vertical loading direction. This could be explained by the grain orientation effect. As shown in Fig. 5, the fine equiaxed grains generally present a random orientation, while the coarse and columnar grains show a slight <001> texture along the building direction (also the vertical loading direction). It has been shown that the <001> orientation leads to the lowest strength for FCC metal [43]. Therefore, the coarse grains exhibiting this orientation would be more prone to deformation in the vertical loading direction, leading to more pronounced strain concentration for both the AB and HT states.

4.3 Anisotropy in ductility

The tensile tests performed in the present work show a notable anisotropy in ductility for both the AB and HT samples (see Fig. 9). The strain at fracture in the horizontal direction is more than twofold that in the vertical direction (Table 3). Such anisotropy is closely related to the damage behavior of the LPBF AA7075-Zr samples. As shown in Figs. 21 and 23, the large and sharp LoF defects accelerate the fracture of the vertical samples, whereas the failure of the horizontal samples is assisted by only small round gas pores as the LoF defects are mostly parallel to the loading direction (Fig. 8). Similar LoF defect features in LPBF AlSi10Mg are demonstrated by Wu et al. [47], where the authors have nicely shown the role of such defects on anisotropic failure by in-situ synchrotron radiation X-ray tomography.

The sharp solidification cracks (parallel to the building direction) may also lead to premature failure of horizontal samples. However, these defects are much sparser and shorter compared to the LoF counterparts (Fig. 8).

The detrimental effect of these LoF defects on ductility shows the need to further refine the process optimization. Indeed, it was shown in our earlier work that, using the same processing parameters, no large LoF pores were detected on small (10 mm × 10 mm × 5 mm) samples [29]. When processing plates dedicated for tensile sample machining (see Fig. 2c), a significant amount of LoF defects was present in the microstructure, as observed in this work. Since these LoF defects are detrimental for ductility, as a perspective of the present work, the LPBF process parameters should be further optimized for plate geometry to suppress LoF defects.

4.4 Maintenance of ductility after HT

A notable finding of the present work is that the ductility is maintained after the T6 heat treatment, despite a significant improvement of the yield strength (roughly by 30%). Such phenomenon has also been reported in previous works [13, 18], but the underlying mechanisms have not been explored. According to the evolutions of the microstructure, defects and the corresponding changes of the microscale strain distribution before and the after the HT, the “break-through” of the strength-ductility tradeoff is induced by the following factors, as also schematically illustrated in Fig. 24:

(i) The large and sharp pores are mostly located in the CGZ and the mixing zone (i.e. large pores traverse the CGZ and FGZ) (Fig. 8) and their sizes do not change during the HT (Fig. 6c). In the AB state, these defects might experience strain localization accommodated by the CGZ (Figs. 11 and 12), therefore leading to premature failure of the sample. Moreover, the strain concentration at the specific bands may also generate voids or accelerate void growth (see Fig. 23a3 and b4), generating a negative influence on tensile ductility. For the HT state, the higher internal stress is supposed to accelerate the defect extension. Nevertheless, the strain concentration at the CGZ is mitigated or even suppressed (Fig. 20) as microstructure is more homogenous, hence delaying the defect extension. In other words, the delocalization of strain for the defect containing region compensates the high internal stress.

(ii) The tiny gas pores in the FGZ may serve as secondary damage sources that assist the primary pore coalescence [48, 49]. It has been shown that the HT can effectively eliminate the tiny pores (Fig. 7) and therefore delay the coalescence of larger voids resulting from initial sharp pores (Fig. 8), relatively large gas pores (Fig. 6c) and Zr-rich particle fracture (Fig. 6a).

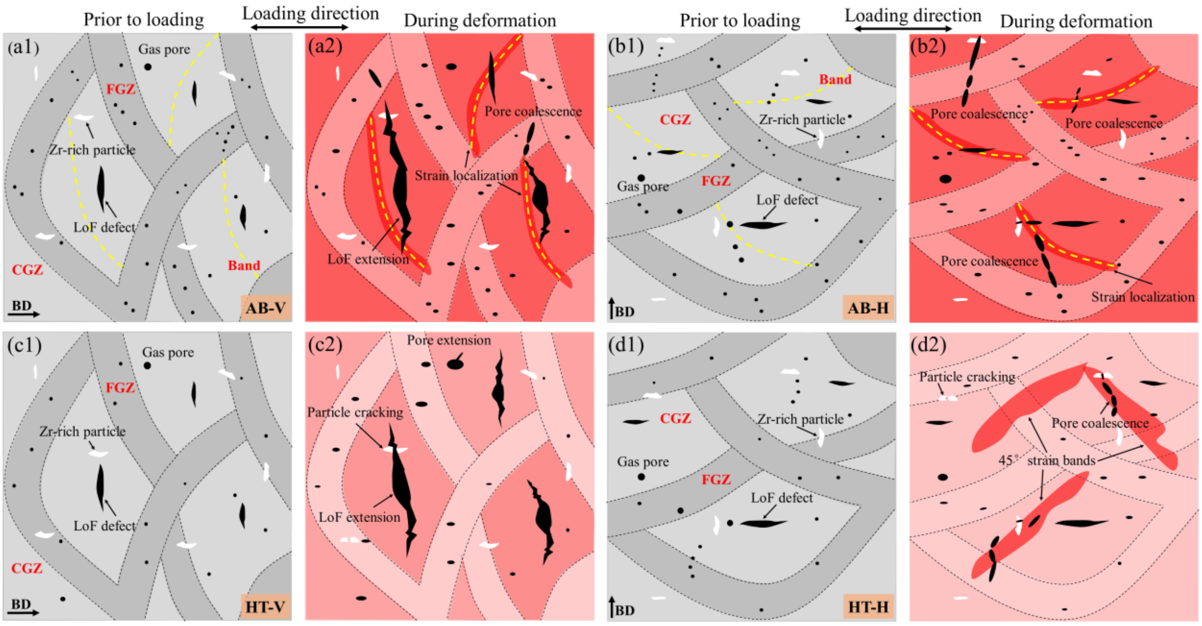

Fig. 24. Schematic drawing of the damage evolution for the AB-V (a1, a2), AB-H (b1, b2), HT-V (c1, c2) and HT-H (d1, d2) samples. The red color depth indicates the strain level.

Moreover, the bimodal grain structure maintained after HT is believed to play an important role in the high ductility. Indeed, it has already been shown in literature for LPBF Al-4Mn-3Ni-2Cu-1Zr [50] and Al-4.58Mn-1.24Mg-0.91Sc-0.42Zr [51] that the CGZ presents a higher ductility compared to the FGZ. Thus, additionally to trapping Zr in solid solution leading to an improved Al_3Zr $L1_2$ hardening after HT [30], the CGZ also contributes to maintain a high ductility. Therefore, the bimodal microstructure is believed to be an asset for reaching an interesting strength-ductility combination for Zr-modified AA7075 processed by LPBF.

5. Conclusions

The present work aims to decipher the structure-mechanical performance relationship of LPBF AA7075-Zr. The microstructure and defects in the as-built state and after the T6 heat treatment were thoroughly characterized. Tensile tests under different loading directions were performed with macroscale and microscale digital image correlation. The main findings are summarized as follows:

(1) The addition of ZrH_2 particles to AA7075 powder in laser powder bed fusion process leads to a bimodal melt pool microstructure, with large columnar grains in the melt pool interiors and fine equiaxed grains at the melt pool borders. The build sample presents large lack of fusion defects preferentially in the coarse grain zone and tiny gas pores preferentially in the fine grain zone.

(2) The as-built material exhibits a heterogeneous strain field, manifested by the significant strain concentration at the coarse grain zones and the specific microstructure bands (a kind of boundary structure separating two coarse grain zones within the melt pool). In contrast, the correlation between the strain distribution and melt pool structure is mitigated after the heat treatment, especially for the horizontal loading direction.

(3) The T6 heat treatment notably modifies the microstructure of the LPBF AA7075-Zr and homogenizes the local mechanical properties. While the large defects (sharp lack-of-fusion pores, Zr-rich particles, etc.) remain nearly unchanged, the submicron (some are even nano-sized) gas pores predominantly located at the fine grain zones are significantly healed by the heat treatment.

(4) Both the as-built and heat treated samples present a ductility anisotropy, which is primarily induced by the large and sharp lack-of-fusion pores lying mostly parallel to the building direction and reducing the ductility in the vertical direction.

(5) The ductility of the as-built samples is retained after the T6 heat treatment despite of the

significant increase in strength. The bypass of strength-ductility trade-off is proposed to be induced by the strain delocalization in the coarse grain zones and the elimination of dense submicron pores.

The present work has shown the potential of additively manufacturing high-strength AA 7075 by adding ZrH_2, with a reasonably good combination of strength and ductility. In the future, more efforts should be devoted to optimize the process parameters to mitigate the long lack-of-fusion defects, which would allow improving the ductility in the vertical direction. Moreover, Mg and Zn loss can be compensated by adding Mg and Zn to the mixed powder (i.e. AA7075 and ZrH_2) to enhance the mechanical strength of the printed sample, especially for the T6 state.

Acknowledgements

L.Z. and Z.L. acknowledge the support from the NSFC (Nos. 12272143 and 12072121). N.N. is a FRIA grantee of the Fonds de la Recherche Scientifique de Belgique FNRS and gratefully acknowledges their support. A.S. and N.N. acknowledge the financial support since 07/2024 from the Win2Wal GreenAl project (convention n° 2310011) funded by the Service public de Wallonie (SPW), Belgium.

Data availability

The data that support the findings of this study are available from the corresponding author upon reasonable request.

References

[1] Q. Liu, H. Ye, J. Cheng, H. Li, X. He, B. Jian, Q. Ge, Stiffness-tunable origami structures via multimaterial three-dimensional printing, Acta Mechanica Solida Sinica 36 (2023) 582-593.

[2] T. DebRoy, H.L. Wei, J.S. Zuback, T. Mukherjee, J.W. Elmer, J.O. Milewski, A.M. Beese, A. Wilson-Heid, A. De, W. Zhang, Additive manufacturing of metallic components - Process, structure and properties, Progress in Materials Science 92 (2018) 112-224.
[3] B. Blakey-Milner, P. Gradl, G. Snedden, M. Brooks, J. Pitot, E. Lopez, M. Leary, F. Berto, A. du Plessis, Metal additive manufacturing in aerospace: A review, Materials & Design 209 (2021) 110008.
[4] G. Liu, X. Zhang, X. Chen, Y. He, L. Cheng, M. Huo, J. Yin, F. Hao, S. Chen, P. Wang, S. Yi, L. Wan, Z. Mao, Z. Chen, X. Wang, Z. Cao, J. Lu, Additive manufacturing of structural materials, Materials Science and Engineering: R: Reports 145 (2021) 100596.
[5] L. Zhao, L. Song, J.G. Santos Macías, Y. Zhu, M. Huang, A. Simar, Z. Li, Review on the correlation between microstructure and mechanical performance for laser powder bed fusion AlSi10Mg, Additive Manufacturing 56 (2022) 102914.
[6] C. Dan, Y. Cui, Z. Chen, H. Liu, G. Ji, Y. Xiao, H. Chen, M. Wang, J. Liu, L. Wang, Y. Li, A. Addad, Y. Zhou, S. Ma, Q. Shi, H. Wang, J. Lu, Achieving ultrahigh fatigue resistance in AlSi10Mg alloy by additive manufacturing, Nature Materials 22 (2023) 1182-1188.
[7] N. Kaufmann, M. Imran, T.M. Wischeropp, C. Emmelmann, S. Siddique, F. Walther, Influence of process parameters on the quality of aluminium alloy EN AW 7075 using selective laser melting (SLM), Physics Procedia 83 (2016) 918-926.
[8] W. Stopyra, K. Gruber, I. Smolina, T. Kurzynowski, B. Kuźnicka, Laser powder bed fusion of AA7075 alloy: Influence of process parameters on porosity and hot cracking, Additive Manufacturing 35 (2020) 101270.
[9] W. Reschetnik, J.-P. Brüggemann, M. Aydinöz, O. Grydin, K.-P. Hoyer, G. Kullmer, H. Richard, Fatigue crack growth behavior and mechanical properties of additively processed EN AW-7075 aluminium alloy, Procedia Structural Integrity 2 (2016) 3040-3048.
[10] R. Mertens, S. Dadbakhsh, J. Van Humbeeck, J.-P. Kruth, Application of base plate preheating during selective laser melting, Procedia Cirp 74 (2018) 5-11.
[11] F.C. Liu, A.H. Feng, X. Pei, Y. Hovanski, R.S. Mishra, Z.Y. Ma, Friction stir based welding, processing, extrusion and additive manufacturing, Progress in Materials Science 146 (2024) 101330.
[12] J.H. Martin, B.D. Yahata, J.M. Hundley, J.A. Mayer, T.A. Schaedler, T.M. Pollock, 3D printing of high-strength aluminium alloys, Nature 549(7672) (2017) 365-369.
[13] F. Jiang, L. Tang, H. Ye, Z. Yang, The role of TiH2 on microstructure and mechanical properties of Al–Zn–Mg–Cu alloy fabricated by laser powder bed fusion, Materials Science and Engineering: A 869 (2023) 144819.
[14] Z. Zhu, F.L. Ng, H.L. Seet, W. Lu, C.H. Liebscher, Z. Rao, D. Raabe, S.M.L. Nai, Superior mechanical properties of a selective-laser-melted AlZnMgCuScZr alloy enabled by a tunable hierarchical microstructure and dual-nanoprecipitation, Materials Today 52 (2022) 90-101.
[15] F. Xiao, S. Wang, Y. Wang, D. Shu, G. Zhu, B. Sun, D. StJohn, Niobium nanoparticle-enabled grain refinement of a crack-free high strength Al-Zn-Mg-Cu alloy manufactured by selective laser melting, Journal of Alloys and Compounds 900 (2022) 163427.
[16] P. Shi, A. Jiang, F. Luo, X. Zhang, X. Wei, Y. Wang, X. Li, Y. Long, Study on defects, densification, and microstructural evolution of additively manufactured Al-Zn-Mg-Cu-Hf alloy, Journal of Alloys and Compounds 973 (2024) 172939.
[17] G. Li, B. Tunca, S. Senol, M. Casata, Y. Wu, Z. Chen, K. Vanmeensel, Revealing the precipitation behavior of crack-free TiB2/Al-Zn-Mg-Cu composites manufactured by laser powder Bed fusion, Additive Manufacturing 66 (2023) 103460.
[18] X. Liu, Y. Liu, Z. Zhou, Q. Zhan, Enhanced strength and ductility in Al-Zn-Mg-Cu alloys fabricated by laser powder bed fusion using a synergistic grain-refining strategy, Journal of Materials Science & Technology 124 (2022) 41-52.

[19] Q. Li, G. Li, X. Lin, D. Zhu, J. Jiang, S. Shi, F. Liu, W. Huang, K. Vanmeensel, Development of a high strength Zr/Sc/Hf-modified Al-Mn-Mg alloy using Laser Powder Bed Fusion: Design of a heterogeneous microstructure incorporating synergistic multiple strengthening mechanisms, Additive Manufacturing 57 (2022) 102967.
[20] M. Buttard, G. Martin, P. Harrison, E.F. Rauch, B. Chéhab, P. Jarry, J.-J. Blandin, P. Donnadieu, Evidence that the liquid structure affects the nucleation of the primary metastable L12-Al3Zr in additive manufacturing, Scripta Materialia 226 (2023) 115212.
[21] J.H. Martin, B. Yahata, J. Mayer, R. Mone, E. Stonkevitch, J. Miller, M. O'Masta, T. Schaedler, J. Hundley, P. Callahan, T. Pollock, Grain refinement mechanisms in additively manufactured nano-functionalized aluminum, Acta Materialia 200 (2020) 1022-1037.
[22] Q. Tan, Z. Fan, X. Tang, Y. Yin, G. Li, D. Huang, J. Zhang, Y. Liu, F. Wang, T. Wu, A novel strategy to additively manufacture 7075 aluminium alloy with selective laser melting, Materials Science and Engineering: A 821 (2021) 141638.
[23] X. Li, D. Li, G. Li, Q. Cai, Microstructure, mechanical properties, aging behavior, and corrosion resistance of a laser powder bed fusion fabricated Al–Zn–Mg–Cu–Ta alloy, Materials Science and Engineering: A 832 (2022) 142364.
[24] M. Li, S. Yao, J. Wang, Z. Chen, G. Zhang, S. Zhang, Y. Li, Role of Er on the densification, microstructure and mechanical properties of 7075 aluminium alloys manufactured by laser powder bed fusion, Journal of Materials Research and Technology 20 (2022) 2021-2033.
[25] L. Li, R. Li, T. Yuan, C. Chen, Z. Zhang, X. Li, Microstructures and tensile properties of a selective laser melted Al–Zn–Mg–Cu (Al7075) alloy by Si and Zr microalloying, Materials Science and Engineering: A 787 (2020) 139492.
[26] B. Huang, Y. Liu, Z. Zhou, W. Cheng, X. Liu, Selective laser melting of 7075 aluminum alloy inoculated by Al–Ti–B: Grain refinement and superior mechanical properties, Vacuum 200 (2022) 111030.
[27] T. Yang, X. Chen, T. Liu, H. Wei, Z. Zhu, Y. Du, Y. Cao, C. Zhang, W. Liao, Crack-free high-strength AA-7075 fabricated by laser powder bed fusion with inoculations of metallic glass powders, Materials Science and Engineering: A 891 (2024) 145916.
[28] J.K. Yoder, R.J. Griffith, H.Z. Yu, Deformation-based additive manufacturing of 7075 aluminum with wrought-like mechanical properties, Materials & Design 198 (2021) 109288.
[29] N. Nothomb, I. Rodriguez-Barber, M.T. Pérez-Prado, N. Jimenez Mena, G. Pyka, A. Simar, Understanding the effect of pre-sintering scanning strategy on the relative density of Zr-modified Al7075 processed by laser powder bed fusion, Additive Manufacturing Letters 11 (2024) 100253.
[30] N. Nothomb, I. Rodriguez-Barber, M. Avettand-Fenoel, M. Pérez-Prado, M. Marinova, A. Simar, Understanding the effect of a tailored heat treatment on Al7075 processed by laser powder bed fusion, Under review (2024).
[31] G. Martinez-Criado, J. Villanova, R. Tucoulou, D. Salomon, J.-P. Suuronen, S. Laboure, C. Guilloud, V. Valls, R. Barrett, E. Gagliardini, Y. Dabin, R. Baker, S. Bohic, C. Cohen, J. Morse, ID16B: a hard X-ray nanoprobe beamline at the ESRF for nano-analysis, Journal of Synchrotron Radiation 23 (2016) 344-352.
[32] P. Cloetens, W. Ludwig, J. Baruchel, D. Van Dyck, J. Van Landuyt, J.P. Guigay, M. Schlenker, Holotomography: Quantitative phase tomography with micrometer resolution using hard synchrotron radiation x rays, Applied Physics Letters 75 (1999) 2912-2914.
[33] A. Mirone, E. Brun, E. Gouillart, P. Tafforeau, J. Kieffer, The PyHST2 hybrid distributed code for high speed tomographic reconstruction with iterative reconstruction and a priori knowledge capabilities, Nuclear Instruments and Methods in Physics Research Section B: Beam Interactions with Materials and Atoms 324 (2014) 41-48.

[34] P.S. Phani, W.C. Olivier, A critical assessment of the effect of indentation spacing on the measurement of hardness and modulus using instrumented indentation testing, Materials & Design 164 (2019) 107563.
[35] J.P.M. Hoefnagels, M.P.F.H.L.v. Maris, T. Vermeij, One-step deposition of nano-to-micron-scalable, high-quality digital image correlation patterns for high-strain in-situ multi-microscopy testing, Strain 55 (2019) e12330.
[36] T. Vermeij, J.P.M. Hoefnagels, Plasticity, localization, and damage in ferritic-pearlitic steel studied by nanoscale digital image correlation, Scripta Materialia 208 (2022) 114327.
[37] J. Blaber, B. Adair, A. Antoniou, Ncorr: Open-Source 2D Digital Image Correlation Matlab Software, Experimental Mechanics 55(6) (2015) 1105-1122.
[38] A.B. Spierings, K. Dawson, K. Kern, F. Palm, K. Wegener, SLM-processed Sc- and Zr- modified Al-Mg alloy: Mechanical properties and microstructural effects of heat treatment, Materials Science and Engineering: A 701 (2017) 264-273.
[39] J. Gheysen, A. Kashiwar, H. Idrissi, J. Villanova, A. Simar, Suppressing hydrogen blistering in a magnesium-rich healable laser powder bed fusion aluminum alloy analyzed by in-situ high resolution techniques, Materials & Design 231 (2023) 112024.
[40] Z. Wu, S. Wu, J. Bao, W. Qian, S. Karabal, W. Sun, P.J. Withers, The effect of defect population on the anisotropic fatigue resistance of AlSi10Mg alloy fabricated by laser powder bed fusion, International Journal of Fatigue 151 (2021) 106317.
[41] G.E. Dieter, Mechanical metallurgy, SI metric edition ed., McGraw-Hill Book Co, New York, 1988.
[42] J. Ganesh Kumar, M. Nandagopal, P. Parameswaran, K. Laha, M.D. Mathew, Effect of notch root radius on tensile behaviour of 316(N) stainless steel, Materials at High Temperatures 31 (2014) 239-248.
[43] K. Zhu, L. Song, L. Zhao, Y. Zhu, S. Liang, M. Huang, Z. Li, Numerical study on the effect of crystallographic orientation on mechanical behavior and its anisotropy of laser powder bed fusion AlSi10Mg, Journal of Alloys and Compounds 976 (2024) 173284.
[44] M. Lezaack, F. Hannard, L. Zhao, A. Orekhov, J. Adrien, A. Miettinen, H. Idrissi, A. Simar, Towards ductilization of high strength 7XXX aluminium alloys via microstructural modifications obtained by friction stir processing and heat treatments, Materialia 20 (2021) 101248.
[45] L. Song, L. Zhao, L. Ding, Y. Zhu, S. Liang, M. Huang, A. Simar, Z. Li, How heterogeneous microstructure determines mechanical behavior of laser powder bed fusion AlSi10Mg, Materials Science and Engineering: A 909 (2024) 146845.
[46] Y. Otani, N. Takata, A. Suzuki, M. Kobashi, M. Kato, Effect of heat treatments on inhomogeneous deformation of the melt-pool structure of Al–Si alloy manufactured via laser powder bed fusion, Materials Science and Engineering: A 909 (2024) 146808.
[47] Z. Wu, S. Wu, X. Goa, Y. Lin, Y. Xue, P.J. Withers, The role of internal defects on anisotropic tensile failure of L-PBF AlSi10Mg alloys, Scientific Reports 13 (2023) 14681.
[48] D. Fabrègue, T. Pardoen, A constitutive model for elastoplastic solids containing primary and secondary voids, Journal of the Mechanics and Physics of Solids 2008 (2008) 719-741.
[49] C. Tekoglu, Void coalescence in ductile solids containing two populations of voids, Engineering Fracture Mechanics 147 (2015) 418-430.
[50] M. Buttard, B. Chehab, C. Josserond, F. Charlot, P. Lhuissier, X. Bataillon, A. Deschamps, J. Villanova, M. Fivel, J. Blandin, G. Martin, Influence of microstructure heterogeneity on the tensile response of an aluminium alloy designed for laser powder bed fusion, Acta Materialia 269 (2024) 119786.
[51] D. Bayoumy, K. Kwak, T. Boll, S. Dietrich, D. Schliephake, J. Huang, J. Yi, K. Takashima, X. Wu, Y. Zhu, A. Huang, Origin of non-uniform plasticity in a high-strength Al-Mn-Sc based alloy produced by laser powder bed fusion, Journal of Materials Science & Technology 103 (2022) 121-133.